Cell Reports
Methods

Article

Microfluidics-enabled proteomic profiling reveal iron-driven immune evasion by an antimicrobial-resistant pathogen

Graphical abstract

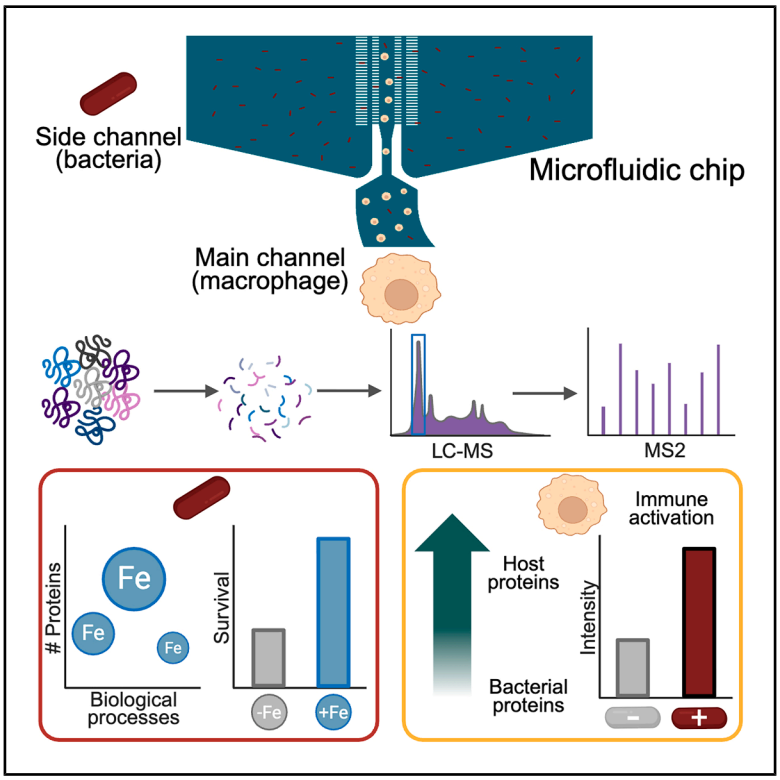

Highlights

- Microfluidic chip enables label-free separation of macrophages and *K. pneumoniae*
- Chip-based proteomics improves immune protein coverage and host-pathogen resolution
- Iron-associated proteins drive bacterial evasion of macrophage phagocytosis
- Workflow reduces handling and cross-contamination and preserves cell viability

Authors

Chikim Nguyen, Chelsea Reitzel, Arjun Sukumaran, Kristina A. Ganzinger, Jennifer Geddes-McAlister

Correspondence

k.ganzinger@amolf.nl (K.A.G.), jgeddesm@uoguelph.ca (J.G.-M.)

In brief

Nguyen et al. introduce a microfluidic-proteomics workflow that separates immune cells from bacteria during infection. This approach reveals how *Klebsiella pneumoniae* uses iron-associated proteins to evade macrophage clearance, providing a powerful way to study host-pathogen interactions and uncover mechanisms of immune escape.

Nguyen et al., 2026, Cell Reports Methods *6*, 101377
May 18, 2026
https://doi.org/10.1016/j.crmeth.2026.101377

CellPress

Cell Reports Methods

CellPress
OPEN ACCESS

Article

Microfluidics-enabled proteomic profiling reveal iron-driven immune evasion by an antimicrobial-resistant pathogen

Chikim Nguyen,[1,3] Chelsea Reitzel,[2,3] Arjun Sukumaran,[2,3] Kristina A. Ganzinger,[1,*] and Jennifer Geddes-McAlister[2,4,*]
[1]Autonomous Matter Department, AMOLF, 1098 XG Amsterdam, the Netherlands
[2]Molecular and Cellular Biology, University of Guelph, Guelph, ON N1G 2W1, Canada
[3]These authors contributed equally
[4]Lead contact
*Correspondence: k.ganzinger@amolf.nl (K.A.G.), jgeddesm@uoguelph.ca (J.G.-M.)
https://doi.org/10.1016/j.crmeth.2026.101377

MOTIVATION Understanding the molecular dialogue between hosts and pathogens remains a major challenge, as infection models often contain heterogeneous cell populations that are difficult to separate without perturbing biological interactions. Conventional approaches rely on labeling or broad separation techniques that can disrupt cells, obscure population-specific responses, and limit mechanistic insight. These limitations are particularly problematic when studying bacterial immune evasion strategies that depend on distinct pathogen subpopulations during infection. Therefore, improved approaches are needed to resolve host and pathogen cells while preserving their native states. Integrating microfluidic cell separation with high-resolution proteomics offers a promising strategy to disentangle complex infection dynamics and uncover molecular mechanisms that govern pathogen survival and host defense.

SUMMARY

Dissecting host-pathogen interactions is challenging due to heterogeneous co-cultures and limited separation methods. Here, we developed a label-free microfluidic chip enabling reproducible separation of *Klebsiella pneumoniae* and murine macrophages during co-culture for high-resolution proteomic analysis. Using an optimized 1.4 μm filter, the platform preserved cell viability while improving host protein identification and enriching immune-associated proteins compared to traditional scraping and supernatant collection. Chip-isolated non-phagocytosed bacteria displayed distinct proteome profiles, including reduced metabolic enzymes and increased biosynthetic and iron-binding proteins. Iron-associated proteins were uniquely enriched in this population, and functional assays confirmed that iron promotes macrophage evasion and bacterial survival. Together, these results establish a microfluidic-proteomic workflow for resolving complex host-pathogen dynamics and propose an iron-dependent mechanism of immune evasion. This approach reduces sample handling and cross-contamination while preserving cellular structure, providing a powerful framework for studying infection biology and identifying therapeutic targets.

INTRODUCTION

The study of host-pathogen interactions is critical to understand how a pathogen evades host immune responses and how a host defends itself from invasion to combat subsequent disease. To study these dynamics, typical methodologies rely on the use of *in vitro* (e.g., cell culture) or *in vivo* (e.g., serum or blood) techniques, which combine cell populations into a single mixture. For drug discovery, the heterogeneity of cell populations makes defining cell-type-specific responses, such as the activation or repression of specific immune cells, challenging without *a priori* knowledge and labeling of populations of interest.[1–4] During infection, exploring differences in pathogen populations, such as pathogen cells that are phagocytosed and lysed versus those that remain viable, or gaining insight into pathogen evasion mechanisms by studying cell populations that are not recognized by the immune system are valuable to better understand regulators of pathogenesis and identify strategies to overcome infection.[5–8]

For the bacterial pathogen *Klebsiella pneumoniae*, invasion of an immunocompromised host promotes bacterial growth and survival during infection, as the immune system is unable to effectively defend itself and clear an infection.[9–11] Commonly associated with nosocomial infections, *K. pneumoniae* infiltrates

the upper respiratory or gastrointestinal tracts of an individual, to cause various infections (e.g., pneumonia, sepsis). The ability of *K. pneumoniae* to cause disease is regulated by several virulence factors, including a polysaccharide capsule, the production of siderophores, and maintaining nutrient homeostasis.[12,13] We previously explored the connection between nutrient homeostasis for metal ions and bacterial virulence, revealing roles in signaling cascade activation and regulation of virulence factor production.[14–17] Perturbation of these factors poses an opportunity to inhibit bacterial virulence (i.e., anti-virulence) and promote clearance by the host's immune system.[18–20] Furthermore, the emergence of hypervirulent and multi-drug-resistant strains exasperates clinical manifestations by limiting current treatment options and raises the need for therapeutic strategies, such as anti-virulence approaches, which disarm the pathogen and can be used in combination with current antimicrobials.[21–25]

To tease apart components influencing host-pathogen interactions, standard methods for separation of cell populations include label-free methods, such as size exclusion chromatography, which separates based on size, or label-based methods, such as flow cytometry, which requires tagging or staining of individual cell types.[26] These strategies enable cell-type-specific separation of populations for further investigation; however, separation specificity is broad and requires additional experimental manipulation for labeling, and the time required for separation can jeopardize stability and detection of biological interactions. To overcome these limitations, recent developments in microfabrication suggest that microfluidic technologies may provide a promising tool for separating cells based on intrinsic properties with a high level of automation at decreased costs.[27–29] Advances in microfabrication allow a broad range of physical principles to be exploited for cell sorting, ranging from microscale filters to hydrodynamic focusing, and field-based techniques (e.g., dielectrophoresis).[30,31] Once separated, the cell populations can be studied using a plethora of methodologies, such as mass-spectrometry-based proteomics, to understand the dynamics of immune system activation or pathogen evasion strategies.[32–35]

In the present study, we designed a microfluidic chip for specific and reproducible separation of pathogen cells from macrophages based on size to define distinguishing features across diverse cell populations. We combined this cell separation technique with high-resolution mass-spectrometry-based proteomics to explore protein-level differences from both the host and pathogen perspectives. We established a *K. pneumoniae* co-culture with immortalized murine BALB/c macrophages and profiled the proteome using traditional methods of cell scraping and supernatant collection versus the chip-based method. Our results show an optimal chip insert filter size of 1.4 μm for reliable separation between bacterial and host cells and maintained cellular viability. The global proteome showed anticipated clustering based on condition, and host profiling revealed consistent differences in macrophage proteome between traditional and chip-based separation techniques. We also detected classical virulence-associated bacterial proteins, including outer membrane proteins, capsule- and siderophore-associated proteins, and lipopolysaccharide export proteins, supporting the validity of our co-culture model under *in vitro*[18,36,37] and *in vivo*[38] conditions. Importantly, using the chip-based separation technique, we observed improved host protein identification rates, increased detection of significant differences between conditions, and enhanced coverage of immune associated proteins. For *K. pneumoniae*, using both traditional (i.e., supernatant) and chip-based (i.e., side channel) methods, we separated bacterial cell populations into non-phagocytosed vs. phagocytosed (or associated) populations and observed a significant increase in bacterial protein identification and a reduction in host proteins following the chip-based method. Further exploration into protein-level changes of non-phagocytosed *K. pneumoniae* collected from the microfluidic chip side channel compared to *K. pneumoniae* not exposed to macrophage revealed decreased abundance of energy-associated proteins (e.g., tricarboxylic acid (TCA) cycle, metabolism, and oxidative phosphorylation) and increased abundance of biosynthesis-associated proteins (e.g., amino acids and secondary metabolites). Additionally, evaluation of proteins exclusively detected within the side channel (not detected under *K. pneumoniae in vitro* conditions) uncovered an enrichment of metal-ion binding and iron-associated proteins. We validated the role of iron in promoting bacterial evasion of macrophage phagocytosis and enhanced bacterial survival to uncover a previously unreported mechanism of immune cell evasion by the *K. pneumoniae* Kp52.145 strain. The use of our microfluidics workflow also decreased sample handling requirements and reduced cross-contamination while preserving cellular structure and improving temporal resolution. Together, we provide a technique to separate host and pathogen cells during co-culture and apply mass-spectrometry-based proteomics to delve deeper into mechanisms regulating the outcome of infectious disease.

RESULTS

Co-cultures of immortalized murine macrophages and bacteria are optimally separated using a crossflow filter channel height of 1.4 μm

To increase our ability to interrogate the dynamics of host-pathogen interactions, we developed a microfluidic chip integrating a crossflow filter system to separate macrophages and bacteria during co-culture based on their size difference. The chip consists of a single inlet connected to four similar separator channel systems arranged in parallel. Each separator consists of one main channel with two series of crossflow filter channels on each side (Figure 1A; Figure S1). Once a co-culture sample is injected into the inlet, the cells pass through the main channels, with only the smaller bacterial cells entering the side channels through the crossflow filters. The length of the channels is designed to ensure that the transit time is sufficiently long to allow most bacteria to enter the side channels and hence be separated from the macrophages remaining in the main channel.

First, we aimed to establish the optimal filter channel height for preventing macrophages from entering the side channels while keeping the channels as large as possible to prevent clogging of the crossflow filter. We found that for channel heights of 4.5 μm, macrophages could easily pass through the crossflow filter (Figure S2), making it impossible to separate macrophages from bacterial cells. Decreasing the height to 3.5 μm, most

CellPress
OPEN ACCESS

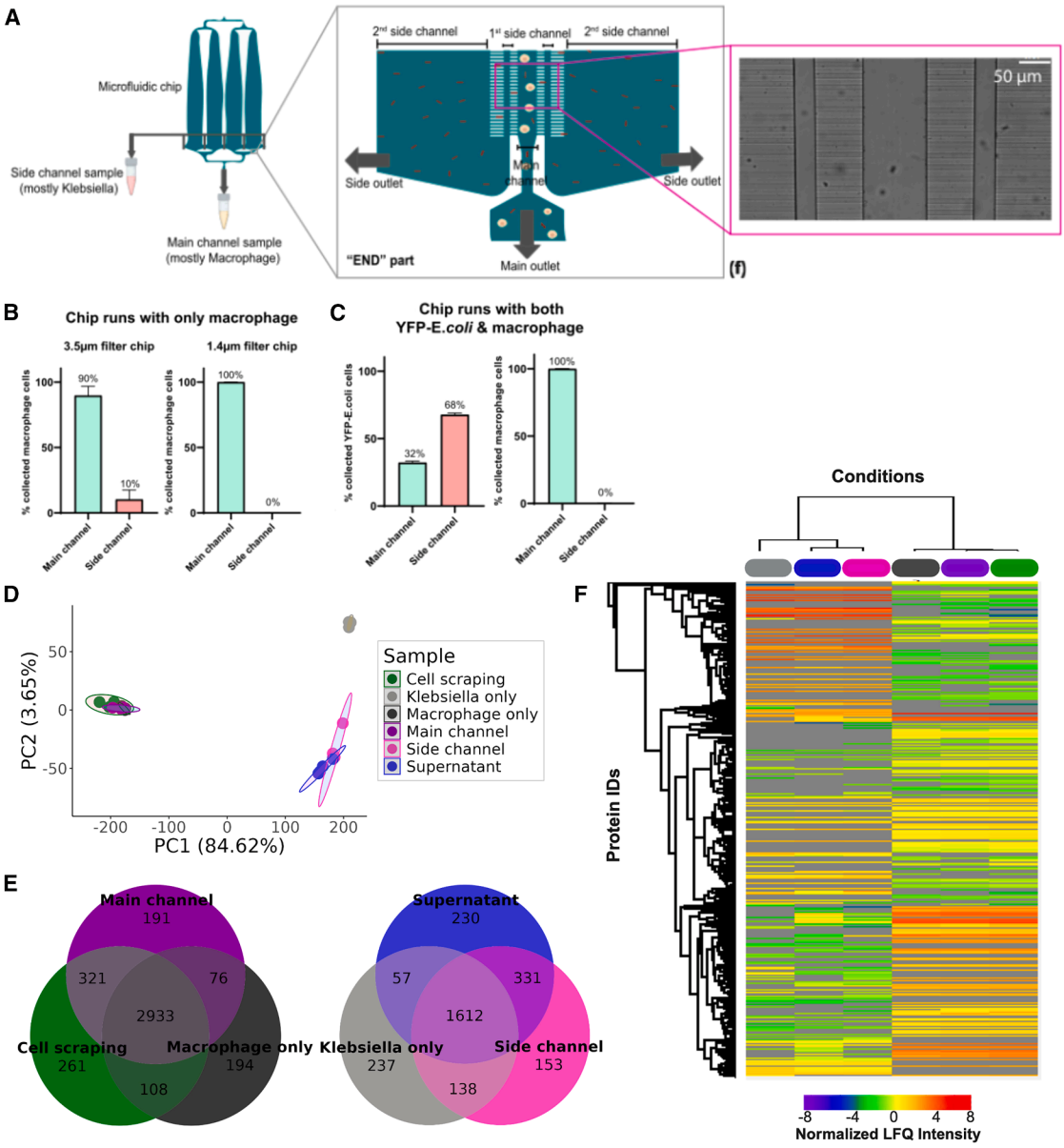

Figure 1. Evaluation of optimal microfluidic chip filter heights and profiling of *K. pneumoniae* and macrophage co-cultures demonstrate global proteome remodeling

(A) Illustration of the microfluidic chip construction designed for collection of immortalized BALB/c macrophage (main channel) and bacteria (side channel). Microscope image of channels. Side channel filter height of 1.4 µm determined to be optimal for *K. pneumoniae* separation from macrophage and collection.

(B) Collection of macrophages from main and side channels with 3.5 µm and 1.4 µm side channel filter height. Mean and standard deviation presented.

(C) Collection of macrophages and YFP-*E. coli* from main and side channels with 1.4 µm side channel filter height. Values of 32% and 68% represent relative percentages of bacteria recovered from the initial input of 10^8 cells from the main and side channels, respectively. Mean and standard deviation presented.

(D) Principal-component analysis across sample sets. Traditional approaches: cell scraping (green) and supernatant (blue) collection. Chip-based separation: main (purple) channel and side (pink) channel. Non-co-cultured samples: macrophage (dark gray) and *K. pneumoniae* (light gray).

(E) Venn diagrams of macrophage proteins detected from cell scraping, main channel, and macrophage samples. Venn diagram of *K. pneumoniae* proteins detected from supernatant, side channel, and *K. pneumoniae* samples. Four biological replicates, averaged with valid value filter of proteins identified in three out of four replicates.

(F) Hierarchical clustering based on Euclidean distance of normalized label-free quantification intensity for identified proteins across all conditions. Four biological replicates, averaged with valid value filter of proteins identified in three out of four replicates. *K. pneumoniae* (light gray), supernatant (blue), side channel (pink), macrophage (dark gray), main channel (purple), and cell scraping (green). Color legend as indicated, and gray = protein not detected. Measured in biological quadruplicate.

macrophages could not enter the crossflow filter anymore, but a small number of cells (around 10% of the collected macrophages) still passed the filters and were collected in the side-channel outlets (Figure 1B; Figures S3 and S4). As the chips were designed with two series of crossflow filters in series, especially for crossflow filters of 3.5 μm height, many macrophages were trapped between the two sets of filters. To improve separation further, we developed chips with smaller filter channel heights of 1.4 μm. For these chips, macrophages did not enter the side channels and were detected only within the main channel (Figure 1B). Notably, macrophages collected from the main channel had high viability (>70%) and retained their original shape (Figure S5).

Knowing that macrophages were collected in the main channel outlet of the 1.4 μm filter chip, we tested if YFP-tagged *Escherichia coli* (straight rod shape, length of 1–2 μm, and diameter of about 1 μm, as determined by microscopy[39]) with a size and shape comparable to *K. pneumoniae* (straight rod shape, length of 0.6–6 μm, and diameter of 0.3–1 μm, as determined by microscopy) could pass the filter and enter the side channels (bacterial physiology confirmed by microscopy). When a suspension of YFP-*E. coli* cells was pumped through the chips, we observed that the bacteria could easily pass through the filters (Video S1). While in the main channel, YFP-*E. coli* moved at a relatively high speed so that single cells were not resolvable by eye, and speed of flow decreased after passing the crossflow filters so that single cells could be observed to enter the side channels and move toward the side channel outlet's direction.

Next, we tested the performance of the chip in separating mixtures of macrophage and YFP-*E. coli* cells. We observed approximately 32% of bacteria (relative amount from starting culture of 10^8 bacteria cells) were recovered from the main channel while 68% (relative amount from starting culture of 10^8 bacteria cells) were recovered from the side channel outlets (Figure 1C). In contrast, all macrophages were collected from the main channel outlet (100%); only very few morphologically altered macrophages were detected in the side channels (Figure S6), in agreement with the previous experiments on samples containing only macrophages (Figure 1B; Figure S5). We, thus, conclude that crossflow filter channel heights of 1.4 μm are optimal for separating mouse macrophages from bacteria within an *in vitro* co-culture setting.

Comparable global proteomes of macrophage and *K. pneumoniae* revealed by traditional and chip-based separation techniques

Following our development and optimization of a microfluidic chip to separate host and bacterial cells within a co-culture, we aimed to compare global proteome coverage and abundance profiles across traditional (i.e., cell scraping and supernatant) and chip-based (i.e., main and side channels) separation techniques. A global look at the data by principal-component analysis revealed separation by component 1 (84.6%) based on host vs. bacterial proteome presence and component 2 (3.7%) by bacterial response to its environment (i.e., growth media only or the presence of macrophages) (Figure 1D). A calculation of correlation across replicates within each condition showed high reproducibility: macrophage-only at 97.0%, cell scraping at 91.5%, main channel at 95.7%, *K. pneumoniae*-only 96.8%, supernatant at 94.0%, and side channel at 94.1% (Figure S7). Notably, although all replicate reproducibility values exceed 90%, there is a significant increase (p = 9.05e-06) in reproducibility in proteome profiling of samples collected from the microfluidic chip main channel compared to the traditional cell scraping method. Next, an assessment of the number of proteins identified across all samples revealed a core host proteome of 2,933 proteins with 194, 261, and 191 host proteins unique to the macrophage-only, cell scraping, and main channel samples, respectively (Figure 1E). Similarly for *K. pneumoniae*, an assessment of the number of proteins identified across all samples revealed a core bacterial proteome of 1,612 proteins with 237, 230, and 153 bacterial proteins unique to the *K. pneumoniae*-only, supernatant, and side channel samples, respectively (Figure 1E). These data demonstrate a large portion of shared proteins among comparable conditions and highlight the detection of condition-exclusive proteins. Critically, among the *K. pneumoniae* proteins identified within the infection conditions (i.e., main channel, side channel, scraped cells, and supernatant), we identified classical bacterial-virulence-associated proteins, including capsule-associated proteins (e.g., Wzi and MurA-G), outer membrane proteins (e.g., OmpX and SlyB), lipopolysaccharide assembly and export proteins (e.g., LptA-E and RcsF), efflux pumps (e.g., TolC), and siderophore-associated proteins (e.g., CirA and IroN) (Table S1). These data support the validity of our co-culture model. Further evidence of these patterns of protein detection is supported by a heatmap of protein abundances with notable differences in production based on sample condition and exposure to host or bacterial cells (Figure 1F). Together, these data highlight comparability in proteomes of host-pathogen interaction samples derived from traditional (e.g., cell scraping and supernatant collection) vs. chip-based (e.g., main and side channels) sample separation to provide a further foundation for in-depth interrogation.

Chip-based separation improves host protein identification rates, increases detection of significant differences, and enhances coverage of immune-associated proteins

Given the comparable global proteome coverage between traditional and chip-based sample separation techniques, we aimed to evaluate host-specific responses to infection dependent upon cell scraping or chip main channel collection. Using a traditional cell scraping approach to collect macrophage following co-culture with *K. pneumoniae*, we detected 95.4% host proteins and 4.6% bacterial proteins (Figure 2A). A statistical comparison of protein abundances from cell scraping between macrophages co-cultured with *K. pneumoniae* compared to uninfected macrophage, identified 74 host proteins with a significant increase in abundance (p <0.05; false discovery rate [FDR] = 5%) and 58 host proteins with a significant decrease in abundance (Figure 2B; Table S2). Notably, 3,571 host proteins did not show a significant change in abundance. Next, to explore changes in the host immune response upon co-culture with *K. pneumoniae*, we focused on proteins associated with the innate and adaptive immune systems and proteins associated with hypoxia; we observed a significant increase in abundance for

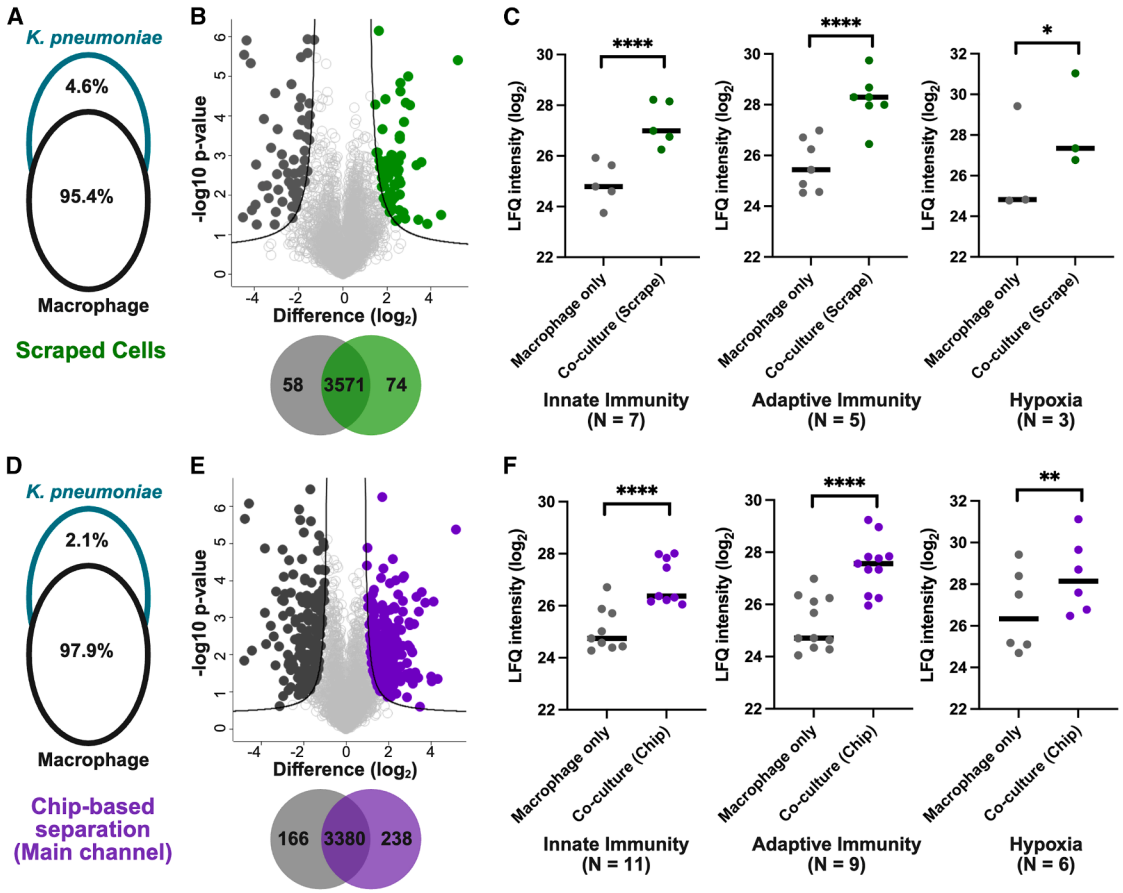

Figure 2. Chip-based separation of macrophages increases total host proteome coverage and provides deeper insights into infection-relevant processes

(A) Percentage of proteins detected from immortalized BALB/c macrophage and *K. pneumoniae* from cell scraping.

(B) Volcano plot of host protein abundance differences between cell scraping (green; right) and macrophage-only (gray; left) samples. Venn diagram illustrates number of statistically significantly different (unpaired Student's *t* test, $p < 0.05$; FDR = 5%; $S_0 = 1$) proteins for cell scraping (green; right), macrophage-only (gray; left), and no significant differences (middle).

(C) Abundance plot of host significantly different proteins associated with innate immune response, adaptive immune response, and hypoxia from cell scraping vs. macrophage-only samples. Unpaired Student's *t* test; $^{*}p < 0.05$, $^{**}p < 0.01$, $^{****}p < 0.001$. Median presented; N = number of significantly different proteins within the designated category.

(D) Percentage of proteins detected from macrophage and *K. pneumoniae* from the chip main channel.

(E) Volcano plot of host protein abundance differences between main channel (purple; right) and macrophage-only (gray; left) samples. Venn diagram illustrates number of statistically significantly different (unpaired Student's *t* test; $p < 0.05$; FDR = 5%; $S_0 = 1$) proteins for main channel (purple; right), macrophage-only (gray; left), and no significant differences (middle).

(F) Abundance plot of host significantly different proteins associated with innate immune response, adaptive immune response, and hypoxia from main channel vs. macrophage-only samples. Unpaired Student's *t* test; $^{*}p < 0.05$, $^{**}p < 0.01$, $^{****}p < 0.001$. Median presented; N = number of significantly different proteins within the designated category. Measured in biological quadruplicate.

each of these categories in the presence of the bacteria (Figure 2C).

Next, to provide a direct comparison of host proteome profiling between the traditional and chip-based separation techniques, we performed the same analysis on proteins detected from the main channel. Here, 97.9% of the proteins detected were assigned to the macrophage, and 2.1% of proteins were designated as *K. pneumoniae* (Figure 2D), showing values comparable to those obtained from cell scarping coverage. A statistical comparison of protein abundances from the chip main channel between macrophages co-cultured with *K. pneumoniae* compared to uninfected macrophages identified 238 host proteins with a significant increase in abundance ($p < 0.05$; FDR = 5%) and 166 host proteins with a significant decrease in abundance (Figure 2E; Table S3). Notably, we identified over 3-fold more significant different proteins in the chip-based vs. cell scraping method; 3,380 host proteins did not show a significant change in abundance. We also assessed changes in the host immune and defense responses between conditions, and as seen with the cell scraping approach, we reported a significant increase in innate and adaptive immunity proteins and hypoxia-associated proteins during exposure to *K. pneumoniae*

(Figure 2F). Importantly, we detected more of these prioritized proteins following assessment of the chip main channel samples compared to the cell scraping approach (Figures 2C and 2F), supporting improved detection of host defenses to bacterial exposure using the microfluidic chip for sample separation.

Chip-based separation of bacterial cells increases proteome coverage and reveals infection-relevant bacterial responses

Following our assessment of the host response to *K. pneumoniae* co-culture under both traditional and chip-based methodologies, we evaluated coverage of the bacterial proteome upon comparison of traditional supernatant vs. chip side channel collection. This strategy enables us to investigate the proteome of non-phagocytosed *K. pneumoniae* cells following their exposure to macrophage. Using a traditional approach to collect supernatant from a macrophage-*K. pneumoniae* co-culture, we detected 73.4% bacterial proteins and 26.6% host proteins compared to collection from the chip side channel where we identified 77.9% bacterial proteins and 22.1% host proteins (Figures 3A and 3B). Interestingly, these values represent a significant (p = 0.0009) increase in the number of *K. pneumoniae* proteins detected across biological replicates from the chip side channel compared to the cell culture supernatant and a minor reduction in host protein identifications (Figure 3C). A summation of the proteome findings upon comparison of traditional cell-scraping vs. microfluidic-enabled profiling is presented (Table 1).

Given this improved coverage of the *K. pneumoniae* proteome from the chip side channel, we further compared changes in protein abundance and production by the bacteria in the presence or absence of macrophage to define proteins with putative roles in evading macrophage detection and/or phagocytosis. First, to confirm that our macrophage co-culture system resulted in phagocytosis of the *K. pneumoniae* strain Kp52.145 despite its hypermucoviscous nature, we used our previously established protocols[18,36,37] and performed colony forming unit counts from co-cultured macrophage (Figure S8). These data support our co-culture system. Next, our experimental design enabled detection of *K. pneumoniae* proteins within the side channel (bacterial proteins exclusively produced following exposure to host cells) and *in vitro K. pneumoniae* culture (with bacteria only) (Figure 3D). We quantified proteins with >2-fold change in abundance under these conditions and discovered 245 bacterial proteins with decreased abundance during exposure to host cells (i.e., putative protein suppression), 196 bacterial proteins with increased abundance during exposure to host cells (i.e., putative protein activation), and 139 bacterial proteins that were only detected following exposure to macrophage (Figure 3E).

Next, we explored protein interaction networks using the STRING database to reveal pathway enrichment based on abundance levels. Specifically, for *K. pneumoniae* proteins with decreased abundance, we observed enrichment of KEGG pathways associated with energy (TCA cycle), metabolism (carbon), oxidative phosphorylation, and lipopolysaccharide biosynthesis (Figure 3F). For *K. pneumoniae* proteins with increased abundance, we observed enrichment of KEGG pathways associated with biosynthesis (amino acid and secondary metabolites) and metabolism (amino acids) (Figure 3G). Lastly, for *K. pneumoniae* proteins exclusively produced upon exposure to macrophages, we observed enrichment of Gene Ontology by Biological Processes (GOBP) associated with biosynthetic processes and metabolic processes. A further assessment of these exclusive proteins by Local Network Cluster (STRING) enrichment defined extensive roles in iron homeostasis, transport, and siderophore biosynthesis (Figure 3I). We explored further and uncovered that 33% of the chip side channel exclusive bacterial proteins had roles in metal acquisition and homeostasis with roles associated with iron accounting for 32%, 72%, and 67% of proteins involved in metal-binding, transport and export, and metabolism, respectively (Figure 3J). Together, these data showed increased coverage of the *K. pneumoniae* proteome following side channel collection using the chip-based approach and revealed regulatory networks suppressed and activated upon bacterial exposure to macrophages. From these data, we proposed a connection between iron homeostasis and protein production in non-phagocytosed *K. pneumoniae*.

Bacterial evasion of macrophage phagocytosis and intracellular survival is driven by increased iron acquisition

Understanding how pathogens evade immune defenses remains a central challenge in infectious disease research. Based on our observations that *K. pneumoniae* exposed to macrophage in co-culture but not phagocytosed (i.e., cells that were collected from the chip side channel showed elevated production of proteins associated with iron homeostasis), we aimed to assess if iron availability influenced bacterial evasion of macrophage. Here, we quantified total cellular iron levels of *K. pneumoniae* strain Kp52.145 incubated in DMEM, supernatant from macrophage (uninfected) cell culture, or supernatant from macrophage exposed to *K. pneumoniae* in co-culture. We observed a significant increase in iron content within *K. pneumoniae* cells following incubation with supernatant from macrophage pre-exposed to the bacterium compared to only DMEM or supernatant from uninfected macrophage (Figure 4A). These findings suggest that cell culture media components, and specifically, components within the media secreted by macrophages following their exposure to *K. pneumoniae*, influence iron uptake by the evaluated *K. pneumoniae* strain.

Using these bacterial samples, we performed quantitative proteomics on cell pellets of *K. pneumoniae* following incubation in supernatant from macrophage (uninfected) cell culture and supernatant from macrophage exposed to *K. pneumoniae* in co-culture. This analysis revealed substantial remodeling of the bacteria upon exposure to co-culture supernatant, with 707 bacterial proteins showing significantly increased abundance and 38 bacterial proteins showing significantly decreased abundance (Figure 4B). A 1D annotative enrichment analysis for changes in protein abundance of all proteins within a defined category[40] revealed significant enrichment of iron-associated protein categories by UniProt Keywords, including 4Fe-4S, iron-sulfur, iron, and metal binding, and by Gene Ontology Molecular Function, including 4Fe-4S cluster binding, metal cluster binding, and iron-sulfur cluster binding (Figure 4C). Notably, a comparison of *K. pneumoniae* proteins identified from the volcano plot data

CellPress
OPEN ACCESS

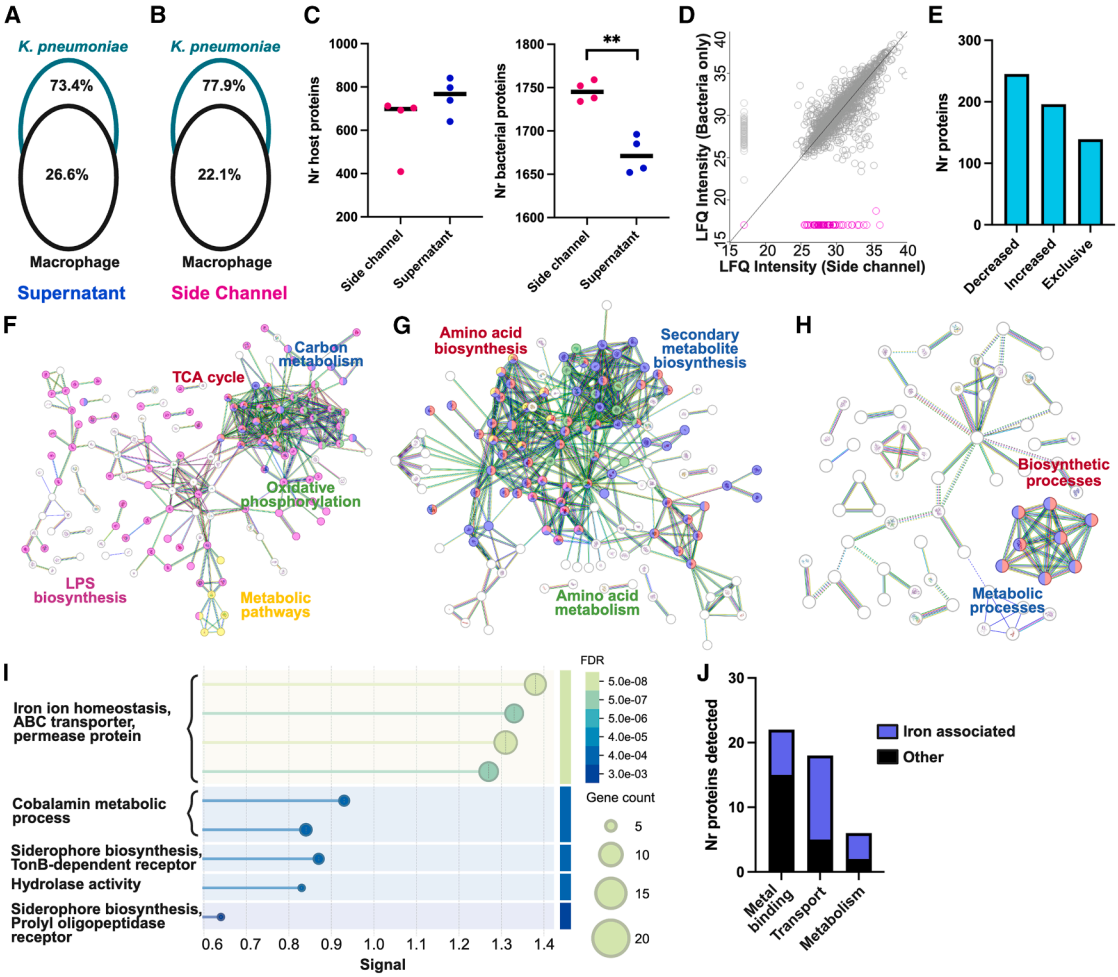

Figure 3. Chip-based separation of *K. pneumoniae* increases total bacterial proteome coverage and defines a role for iron acquisition and homeostasis in non-phagocytosed bacteria

(A) Percentage of proteins detected from immortalized BALB/c macrophage and *K. pneumoniae* from the co-culture supernatant.

(B) Percentage of proteins detected from macrophage and *K. pneumoniae* from the chip side channel.

(C) Comparison of host and bacterial proteins detected between traditional (i.e., supernatant) and chip-based (i.e., side channel) samples. Unpaired Student's *t* test $^{**}p < 0.01$. Mean presented.

(D) Scatterplot of bacterial protein abundances in *K. pneumoniae*-only samples compared to the chip side channel samples. Proteins exclusive to *K. pneumoniae* (light gray) or side channel (pink). LFQ intensity plotted; x = 1. Mean presented.

(E) Number of bacterial proteins with >2-fold decrease or increase in abundance or exclusive to chip side channel vs. *K. pneumoniae*-only samples.

(F) STRING protein-protein interaction map of bacterial proteins with decreased abundance in chip side channel compared to *K. pneumoniae*-only samples. Significantly enriched KEGG pathways colored and labeled.

(G) STRING protein-protein interaction map of bacterial proteins with increased abundance in chip side channel compared to *K. pneumoniae*-only samples. Top five significantly enriched KEGG pathways colored and labeled.

(H) STRING protein-protein interaction map of bacterial proteins exclusively detected in chip side channel compared to *K. pneumoniae*-only samples. Significantly enriched KEGG pathways colored and labeled. For STRING, nodes represent proteins by color (query proteins and first shell interactors) and content (a 3D structure is known or predicted). For STRING, edges represent protein-protein associations by known interactions (blue = curated databases, pink = experimentally determined), predicted interactions (green = gene neighborhood, red = gene fusions, blue = gene co-occurrence), or others (gray = text mining, black = co-expression, gray/blue = protein homology). Minimum required interaction score = high confidence (0.700). Protein names and disconnected nodes are not shown.

(I) Functional enrichment based on Local Network Cluster (STRING) enrichment for bacterial proteins exclusively detected in chip side channel compared to *K. pneumoniae*-only samples. Group terms by similarity >0.8; sort terms by signal.

(J) Number of metal-associated proteins exclusively detected in chip side channel compared to *K. pneumoniae*-only samples; number of proteins with roles associated with "iron" separated from total. Measured in biological quadruplicate.

Table 1. Summation of proteome profiling findings between traditional vs. microfluidic-enabled approaches

	Processing time (min)[a]	Replicate reproducibility	# proteins	% host/bacteria proteins	# Sig. diff. proteins
Macrophage					
Cell scraping	90 + S/N + 3 + 1 + 5 + 1 = 100 + S/N	91.5%	3,194	95.4%/4.6%	132
Main channel	90 + 1 + 50 + 5 + 1 = 147	95.7%	3,124	97.9%/2.1%	404
K. pneumoniae					
Supernatant	90 + 1 + 5 + 1 = 97	94.0%	1,842	26.6%/73.4%	N/A
Side channel	90 (+ 1 + 50) + 5 + 1 = 96 (+51)	94.1%	1,765	22.1%/77.9%	N/A

[a]90 min = co-culture; S/N = processing supernatant; 3 = wash cells with PBS and release cells with detergent; 1 = pipetting to remove/collect liquid; 5 = centrifugation; 50 = microfluidic chip flow; brackets indicate simultaneous procedure.

with significant changes in abundance and defined roles as metal co-factors showed elevated production upon exposure to supernatant from co-culture (infected; 136 bacterial proteins) compared to supernatant collected from macrophage-only (uninfected; five bacterial proteins) samples (Figure 4D). These data further support remodeling of the bacterial proteome for increased iron acquisition upon exposure to supernatant from *K. pneumoniae*-infected macrophages.

To explore a mechanistic connection between activation of bacterial iron acquisition systems and bacterial evasion of macrophages, we cultured *K. pneumoniae* in iron-limited (M9 media) vs. iron-supplemented [M9 media supplemented with 10 μM $Fe_2(SO_4)_3$] media and measured total internalized iron of *K. pneumoniae* cells. In line with our previous results, when *K. pneumoniae* was exposed to macrophage co-culture supernatant, we observed a significant increase in internal iron levels within the bacterium upon incubation in iron-supplemented media (Figure 4E). These data show that in the presence of iron within culture media, *K. pneumoniae* will increase acquisition of the metal ion. Next, we co-cultured *K. pneumoniae* (preconditioned in iron-limited or iron-supplemented media) with macrophages and quantified the number of bacteria in the culture supernatant following 90-min incubation. We observed a significant increase in the number of non-phagocytosed *K. pneumoniae* cells following "priming" of the bacteria in culture media supplemented with iron (Figure 4F). These data validate our hypothesis that *K. pneumoniae* exposed to macrophage but not undergoing phagocytosis, as with bacteria "primed" with iron exposure, are less susceptible to macrophage detection and phagocytosis. Finally, co-culturing *K. pneumoniae* (cultured in iron-limited or iron-supplemented media) with macrophage, we enumerated the number of bacteria recovered following attachment or phagocytosis by macrophages. We observed a significant increase in survival of *K. pneumoniae* within macrophage upon prior bacteria exposure to iron-replete conditions (Figure 4G). These data support protection of *K. pneumoniae* both from macrophage phagocytosis and after phagocytosis within macrophages following bacterial cell "priming" with elevated iron levels. Notably, cytotoxicity levels of macrophage (measured by lactate dehydrogenase release) upon exposure to each condition above did not significantly differ (Figure S9). Taken together, these data demonstrate proteome remodeling of *K. pneumoniae* Kp52.145 in the presence of elevated iron to increase production of iron acquisition systems, provide protection from macrophage phagocytosis, and promote bacterial survival within macrophages.

DISCUSSION

We successfully developed and optimized a continuous-flow microfluidic fractionation chip integrating crossflow filters to separate macrophages from *K. pneumoniae* during co-culture based on size differences. Our systematic evaluation of filter channel heights revealed that a critical dimension of 1.4 μm is essential for effective separation, enabling complete exclusion of macrophages from the side channels while allowing a substantial fraction (~66%) of bacteria to pass through. This two-stage filtration performance aligns closely with prior reports demonstrating similar separation efficiencies for red blood cells and *E. coli* at comparable filter heights, supporting the robustness of our design.[29] Importantly, the microfluidic separation preserved cell viability and morphology, confirming that our microchip enables efficient, gentle fractionation of host and pathogen populations with minimal disruption, providing a powerful tool to dissect complex host-pathogen interactions with improved specificity and reproducibility for downstream applications.

The resolution afforded by our microfluidic platform enabled compartmentalized sampling of host and bacterial populations, revealing nuanced patterns of infection-associated protein distribution. While the side channel was designed to isolate bacteria based on size and flow dynamics, we also detected host-derived proteins within this compartment. These host proteins are of particular interest for their putative roles in modulation of infection. For example, cytokines and chemokines are released from macrophage upon pathogen activation to stimulate nearby immune cells, send alert signals to distant regions of the host, and recruit additional immune cells to the site of infection.[41] Notably, host proteins detected within the chip side channel included well-characterized immune response proteins, such as progranulin with defined roles in bacterial survival, macrophages efficacy, and modulation of inflammation[42,43] and complement component 1Q (C1qbp), which initiates the classical complement pathway by binding directly to the surface of bacterial cells.[44] Conversely, bacterial proteins detected in the main channel may originate from multiple sources, including internalized bacteria within phagosomes, bacteria adherent to the macrophage surface, or free bacteria retained within the main flow path due to speed of filtration.

To delineate host immune dynamics during *K. pneumoniae* co-culture, we concentrated on proteins linked to innate and adaptive immunity as well as hypoxia-responsive pathways. The significant upregulation of proteins within these categories underscores a robust immune activation response that

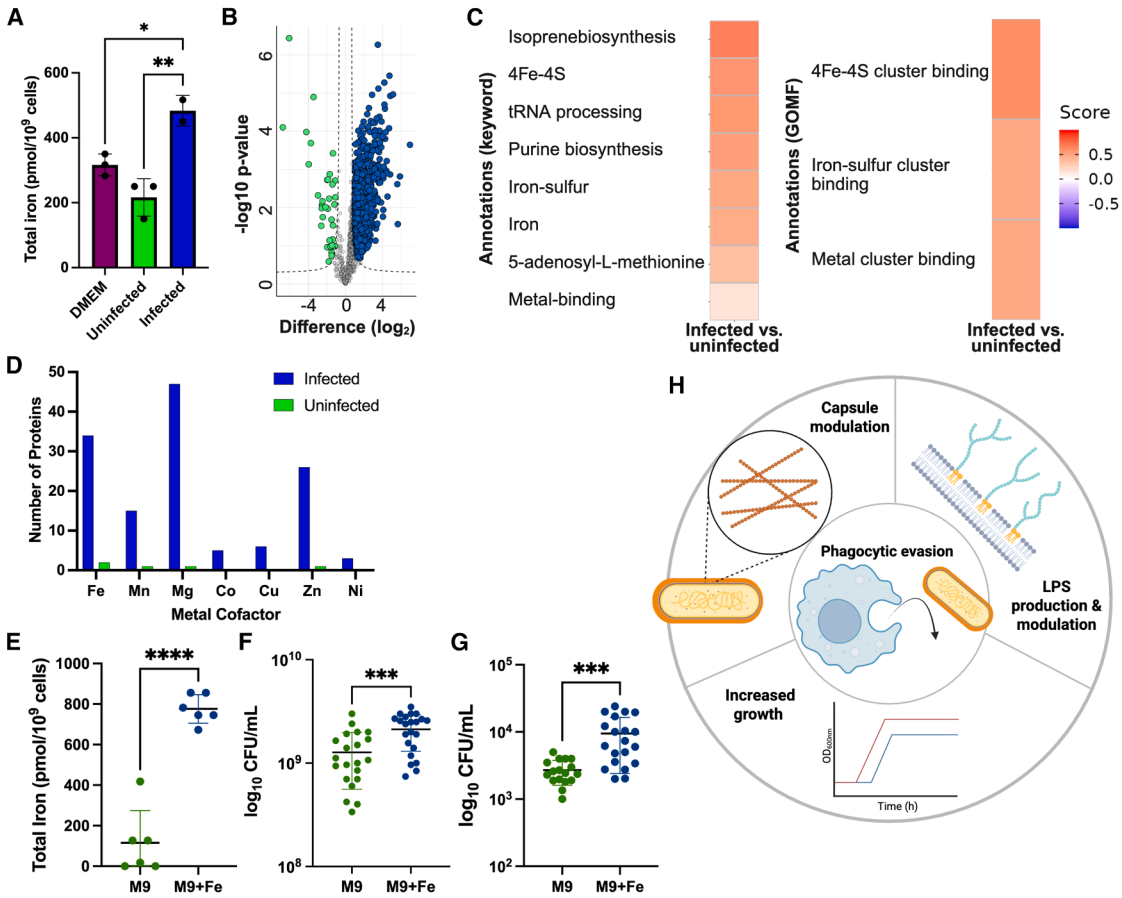

Figure 4. Iron internalization via media or macrophage exposure influences *K. pneumoniae* evasion of phagocytosis

(A) Total iron content (i.e., Fe^{2+} and Fe^{3+}) of 10^9 *K. pneumoniae* cells incubated in DMEM, uninfected immortalized BALB/c macrophage supernatant, or *K. pneumoniae*-infected macrophage supernatant for 2 h. Reported values denote mean of biological triplicate collected in triplicate experiments. Error bars denote standard deviation. Significant difference (*p <0.05; **p <0.01) calculated by unpaired Student's t test.

(B) Volcano plot of *K. pneumoniae* grown in macrophage supernatant from uninfected and *K. pneumoniae*-infected conditions. Proteins with statistically significant changes in abundance are highlighted in blue (i.e., more abundant following bacterial exposure to macrophage supernatant from *K. pneumoniae*-infected samples) or green (i.e., more abundant following bacterial exposure to macrophage supernatant from uninfected samples). Significance by unpaired Student's t test with $p \leq 0.05$, FDR = 0.05, and $S_0 = 1$.

(C) 1D annotation enrichment of proteins detected from *K. pneumoniae* grown in macrophage supernatant from uninfected and *K. pneumoniae*-infected conditions based on UniProt Keywords and Gene Ontology Molecular Function. Statistical analysis by unpaired Student's t test p <0.05; FDR = 5%.

(D) Number of significantly more abundant proteins with known metal cofactors in *K. pneumoniae* grown in macrophage supernatant from uninfected (green) and *K. pneumoniae*-infected (blue) conditions. Protein counts normalized to total number of proteins identified in each condition (i.e., 1,246 proteins identified in *K. pneumoniae* grown in macrophage supernatant from *K. pneumoniae*-infected conditions and 1,149 proteins identified in *K. pneumoniae* grown in macrophage supernatant from uninfected conditions).

(E) Total iron content (i.e., Fe^{2+} and Fe^{3+}) of 10^9 *K. pneumoniae* cells incubated in M9 minimal media or M9 minimal media supplemented with 10 μM $Fe_2(SO_4)_3$. Mean and standard deviation presented.

(F) CFU counts for *K. pneumoniae* in supernatant after 90 min co-culture with BALB/c macrophage (MOI 100:1) following *K. pneumoniae* pre-conditioning in M9 minimal media or M9 minimal media supplemented with 10 μM $Fe_2(SO_4)_3$. Mean and standard deviation presented.

(G) CFU counts for viable phagocytosed *K. pneumoniae* after 90 min co-culture with BALB/c macrophage (MOI 100:1) following *K. pneumoniae* pre-conditioning in M9 minimal media or M9 minimal media supplemented with 10 μM $Fe_2(SO_4)_3$. Mean and standard deviation presented.

(H) Proposed mechanisms supporting *K. pneumoniae* evasion of phagocytosis and enhanced survival.

Reported values are the mean of three biological replicates collected in two independent experiments. Error bars denote standard deviation. Significant difference (***p <0.0002, ****p <0.0001) was calculated using unpaired Student's t test.

encompasses diverse cellular processes. Hypoxia, a hallmark of infected and inflamed tissues, is known to profoundly influence immune cell function and pathogen clearance.[45,46] This is particularly relevant, given recent systems immunology findings implicating metabolic regulators, such as prenylcysteine oxidase 1 (Pcyox1l), in governing neutrophil bactericidal capacity through modulation of pathways like the mevalonate pathway and autophagy processes.[47] Our observations of elevated hypoxia-associated proteins, with a particular interest in detection of significantly differential abundance of Pcyox1l from the

chip-based main channel, which was not observed from the traditional cell scraping approach, suggest that macrophage responses to *K. pneumoniae* involve metabolic reprogramming to sustain effector functions under low-oxygen stress, potentially enhancing antimicrobial defense. The integration of metabolic cues with immune activation aligns with mounting evidence that immune cell efficacy hinges on tightly coordinated metabolic pathways.[48–50] Taken together, these data support a model where infection-induced hypoxia acts as both a stressor and a signal, orchestrating host immune adaptations essential for controlling bacterial pathogens.

Our proteomic analysis revealed a pronounced increase in iron storage and transport proteins in *K. pneumoniae* during macrophage infection, with a plethora of bacterial proteins implicated in iron storage, including iron-sulfur cluster assembly proteins (e.g., lipoyl synthase, fumarate hydratase, and IscA), showing elevated abundance compared to a single iron storage protein, IscR, enriched in uninfected conditions. This increased abundance corresponds with a 4-fold increase in the ferric uptake regulator (Fur) protein, a key transcription factor that orchestrates bacterial iron homeostasis by activating iron storage genes in response to elevated intracellular iron.[51] Complementing these findings, the outer membrane porin OmpF, known for facilitating ferrous iron uptake, was approximately 8-fold more abundant in infected samples.[52] These findings align with our elemental analysis indicating heightened intracellular iron accumulation in *K. pneumoniae* following exposure to supernatant from macrophage co-cultured with the bacterium. Interestingly, a TonB-dependent siderophore receptor (*iroN*) was approximately 6-fold more abundant in uninfected conditions, likely reflecting a shift from siderophore-mediated iron scavenging toward an "iron hoarding" state of bacteria during infection, where iron storage supersedes acquisition to mitigate toxicity risks. This nuanced regulatory response fills a critical knowledge gap, as quantitative iron content at the single-cell level for *K. pneumoniae* has been previously underreported, supplementing existing data typically reported as iron levels per culture volume, colony-forming unit (CFU), or dry cell weight.[53–55] Our data provide a precise measure of iron content normalized by cell number under defined growth conditions, advancing the field's understanding of bacterial iron physiology during host interaction with an emphasis on the evaluated *K. pneumoniae* Kp52.145 strain. As we explored the effects of pre-conditioning on macrophage phagocytosis of *K. pneumoniae*, future experiments could further tease apart the link with iron availability by conducting similar experiments in the presence of iron chelators to further assess the role of iron in immune evasion.

Beyond protein-level adaptations, our results underscore the functional consequences of macrophage-bacteria crosstalk in iron acquisition and immune evasion.[56] Macrophage-secreted factors, including cytokines known to induce bacterial iron acquisition genes,[57,58] appear to prime *K. pneumoniae* for increased iron internalization, as evidenced by elevated bacterial iron levels following exposure to infected macrophage supernatants. This interplay reveals an important facet of the infection microenvironment, where host immune responses inadvertently facilitate bacterial metabolic adaptation. Notably, this study explores how direct bacterial supplementation with nutrient metals, specifically iron, modulates susceptibility to phagocytosis, expanding beyond the traditional focus on host dietary metal supplementation.[59–62] Our findings demonstrate that iron-primed *K. pneumoniae* cells exhibit reduced phagocytic uptake and enhanced intracellular survival, consistent with prior studies that implicate metal availability within the phagolysosome as a determinant of bacterial clearance, while providing a mechanism of immune cell evasion used by *K. pneumoniae*.[63–66]

Although direct experimental evidence is still required to define the precise link between iron acquisition and phagocytic evasion, we propose that iron provides a significant metabolic advantage, given its role as a cofactor in numerous biosynthetic processes for bacteria. We theorize that enhanced iron acquisition confers an adaptive benefit in infection settings where immune cells, such as macrophages, generate iron-limited microenvironments.[67,68] These conditions trigger bacterial cell reprogramming to promote survival adaptations, including phagocytic evasion. We suggest that such reprogramming modulates three major factors: capsule formation, lipopolysaccharides (LPSs), and bacterial growth (Figure 4H). For example, capsule formation is a well-established mediator of immune evasion in bacteria.[69] In iron-limited environments, such as infection settings, bacteria undergo cellular reprogramming that increases capsule production.[70] We propose that bacteria able to acquire iron under these conditions possess greater metabolic capacity to support capsule modulation, thereby enhancing immune evasion. This metabolic capacity is facilitated through the role of iron as a cofactor in cellular respiration, which generates ATP for processes, such as nucleotide sugar synthesis for capsule formation and phosphorylation of Wzc to regulate capsule polymerization and export.[71] Future directions for our microfluidic chip workflow could include comparing capsule thickness between phagocytosed and non-phagocytosed *K. pneumoniae* to test this hypothesis or exploring adjacent biological questions by assessing differences in host response or bacterial adaptability between capsular and acapsular strains.

Another important factor that is modulated by iron is LPS, a potent activator of immune cells. Thus bacteria modulate LPS production to avoid detection and phagocytosis.[72] Under iron-limited conditions, bacteria produce shorter LPS chains and modify lipid A through deacylation and dephosphorylation, thereby reducing recognition by macrophage TLR4–MD2 receptors.[72,73] Notably, we identified a transmembrane protein involved in lipid A phosphatidylethanolamine modification (*yhjW*[74]) uniquely under the phagocytic-evasion conditions, underscoring a connection between lipid A remodeling and immune evasion. Future experiments separating phagocytosed and non-phagocytosed populations may investigate a putative connection between LPS modifications and phagocytic evasion. Additionally, iron acquisition accelerates growth by serving as a cofactor in biosynthetic pathways and facilitating energy generation through electron transfer intermediates. Under infection settings where iron is scarce, bacteria with greater iron stores or enhanced acquisition capacity gain a growth advantage over less iron-rich populations. This advantage may enable bacterial replication at rates that exceed macrophage clearance

capacity. Furthermore, the improved intracellular survival of phagocytosed *K. pneumoniae* pre-conditioned in iron-replete media can be explained by their ability to withstand macrophage-mediated iron starvation.[75] The iron-associated phenomenon of phagocytic evasion mirrors observations in other systems, such as *Agrobacterium tumefaciens*, where exposure to biomass-increasing growth conditions and plant-derived additives primes bacterial virulence gene expression and improves host invasion efficiency.[76–78] Our findings extend this concept to *K. pneumoniae*, suggesting that environmental cues, such as iron availability, can serve as priming signals that prepare bacteria for more effective immune evasion and intracellular persistence. The impact of iron priming on bacterial immune evasion may have significant implications for infection progression and treatment, highlighting the need to consider microbial metabolic state and environmental conditions in therapeutic design. In conclusion, our study presents a microfluidic-proteomic workflow that reveals an iron-dependent mechanism of macrophage evasion by *K. pneumoniae*, offering a powerful tool for dissecting broad-spectrum host-pathogen interactions to identify targets for therapeutic intervention.

Limitations of the study

A notable limitation is the time required to process samples using the microfluidic chip (i.e., 50 min total flow) compared to the traditional method (i.e., approximately 24 min) (Table 1). Despite the increase in time for processing samples, the microfluidic chip enables simultaneous separation of main and side channels, increasing reproducibility within a single experiment, and could be expanded to multiple microfluidic chips to process samples in parallel for increased throughput. Another potential limitation of microfluidic chip processing time are any potential changes to the bacteria or host during the flow rate. As the media (DMEM) is diluted with PBS during chip flow, we note that the increased coverage of the bacterial proteome from the side channel does not correspond with increased bacterial proteins, but rather a reduction in cross-contamination from macrophage proteins. To further evaluate the effect of time, future experiments may collect and process samples as they are separated into the main or side channel, or the *K. pneumoniae*-only samples could be processed through the chip to determine any potential proteome changes induced across time. Finally, as both approaches use cell scraping to remove adherent macrophages from the culture surface prior to processing (traditional method) or separation (microfluidic chip method), physical disruption to the cells is possible, which may introduce variance in cell morphology. Future experiments may establish co-culturing with non-adherent cells to reduce such variance and even enable co-culturing within the microfluidic chip prior to initiation of flow and cell separation.

Another limitation of the microfluidic chip workflow is the inability to separate macrophage populations based on bacterial loads, which could confirm abundance changes in iron efflux proteins, such as Nramp1, in macrophages that had engulfed bacteria.[68] Future microfluidic chip devices could incorporate additional separation-based techniques by morphology changes and surface chemical modifications that occur during phagocytosis to distinguish host cell populations and gain further insights into mechanisms of host response.[58,79,80] Moreover, our analysis focuses on a single host cell type (i.e., murine macrophages), and this observation, although informative and relevant to the infection model studied, is limited in application beyond the evaluated macrophages and provides a foundation to expand to other relevant host immune cell types, such as primary macrophages, neutrophils, dendritic cells, etc.

Future directions for the microfluidic chip workflow could explore how bacterial capsule size influences cell sorting, given the established role of capsule thickness in determining cell size and mediating phagocytosis evasion.[69,70] It is reasonable to hypothesize that bacteria recovered from the main channel (those phagocytosed) possess thinner capsules compared to those sorted into the side channel, as encapsulated *K. pneumoniae* display greater resistance to phagocytosis compared to capsule-deficient bacteria.[81] Beyond the current strain, this workflow could be applied to hypervirulent *K. pneumoniae* or other similarly sized bacteria to assess whether iron-associated proteins are consistently enriched in the phagocytosis-evasion population (i.e., side channel isolates) or whether this phenomenon is strain-specific. Extending the workflow to additional bacterial species (e.g., *Salmonella* spp.), fungal pathogens (e.g., *Cryptococcus neoformans*), and potentially diverse host cell types (e.g., red blood cells and neutrophils), would provide a versatile platform for dissecting host-pathogen interactions. Further, adaptation of the microfluidic chip workflow toward *bona-fide* infection settings, such as the separation of host and pathogen cells from blood or bronchoalveolar lavage, and ultimately, tissue homogenates, presents an exciting and unexplored area for future investigation.

RESOURCE AVAILABILITY

Lead contact

Requests for further information and resources should be directed to and will be fulfilled by the lead contact, Dr. Jennifer Geddes-McAlister (jgeddesm@uoguelph.ca).

Materials availability

The study did not generate new unique reagents.

Data and code availability

- The proteomics datasets are publicly available through PRIDE Proteomics Exchange: PXD058426 and PXD051800.
- This study does not report original code.
- Any additional information required to re-analyze the data reported in this paper is available from the lead contact upon request.

ACKNOWLEDGMENTS

The authors thank members of the Geddes-McAlister and Ganzinger labs for helpful discussions and constructive comments on the study. The authors thank Dr. Boyan Liu and Sam Pladwig (MSc) for experimental technical assistance, Dr. Jason McAlister for bioinformatics training, Dr. Fotios Avgidis for helpful discussions on chip fabrication and microscopy, Dimitry Lamers for assisting AutoCAD design and photolithography training, the Shimizu lab at AMOLF for providing YFP-*E. coli*, and Dr. Dyanne Brewer of the Advanced Analysis Centre of the University of Guelph for operation of the mass spectrometer. This work was supported in part by the Canada Foundation for Innovation (CFI-JELF no. 38798) and NSERC Discovery Grant (RGPIN-2020-04838) for J.G.-M. and the New Frontiers Research Fund: Exploration (NFRFE-2019-00425) for J.G.-M. and K.A.G.

AUTHOR CONTRIBUTIONS

J.G.-M. and K.A.G. conceptualized and designed the study and obtained funding. C.N. designed and constructed the microfluidic chips. A.S. supported experimental design. C.N., C.R., and A.S. performed experiments. C.N., C.R., J.G.-M., and K.A.G. contributed to data analysis, prepared figures, and drafted manuscript. All authors have read and approved the submitted manuscript.

DECLARATION OF INTERESTS

The authors declare no competing interests.

STAR★METHODS

Detailed methods are provided in the online version of this paper and include the following:

- KEY RESOURCES TABLE
- EXPERIMENTAL MODEL AND STUDY PARTICIPANT DETAILS
  - Macrophage cell culture
  - Bacterial strain preparation
  - Co-culturing for macrophage and *K. pneumoniae*
- METHOD DETAILS
  - Microfluidic chip design
  - Master mold fabrication with photolithography
  - PDMS chip fabrication
  - Pre-operation and testing of microfluidic chips
  - Sample collection
  - Sample preparation for proteomic profiling
  - Mass spectrometry
  - Data processing and bioinformatics
  - Iron quantification assay
  - Lactate dehydrogenase cytotoxicity assay
  - Phagocytosis evasion and phagocytosed bacteria viability
- QUANTIFICATION AND STATISTICAL ANALYSIS

SUPPLEMENTAL INFORMATION

Supplemental information can be found online at https://doi.org/10.1016/j.crmeth.2026.101377.

Received: September 12, 2025
Revised: January 3, 2026
Accepted: March 5, 2026
Published: March 30, 2026

REFERENCES

1. Kinnunen, P.C., Humphries, B.A., Luker, G.D., Luker, K.E., and Linderman, J.J. (2024). Characterizing heterogeneous single-cell dose responses computationally and experimentally using threshold inhibition surfaces and dose-titration assays. NPJ Syst. Biol. Appl. *10*, 42. https://doi.org/10.1038/s41540-024-00369-x.
2. Chen, S., Rivaud, P., Park, J.H., Tsou, T., Charles, E., Haliburton, J.R., Pichiorri, F., and Thomson, M. (2020). Dissecting heterogeneous cell populations across drug and disease conditions with PopAlign. Proc. Natl. Acad. Sci. USA *117*, 28784–28794. https://doi.org/10.1073/pnas.2005990117.
3. Gough, A., Stern, A.M., Maier, J., Lezon, T., Shun, T.-Y., Chennubhotla, C., Schurdak, M.E., Haney, S.A., and Taylor, D.L. (2017). Biologically Relevant Heterogeneity: Metrics and Practical Insights. SLAS Discov. *22*, 213–237. https://doi.org/10.1177/2472555216682725.
4. Gough, A.H., Chen, N., Shun, T.Y., Lezon, T.R., Boltz, R.C., Reese, C.E., Wagner, J., Vernetti, L.A., Grandis, J.R., Lee, A.V., et al. (2014). Identifying and Quantifying Heterogeneity in High Content Analysis: Application of Heterogeneity Indices to Drug Discovery. PLoS One *9*, e102678. https://doi.org/10.1371/journal.pone.0102678.
5. Paczosa, M.K., and Mecsas, J. (2016). *Klebsiella pneumoniae*: Going on the Offense with a Strong Defense. Microbiol. Mol. Biol. Rev. *80*, 629–661. https://doi.org/10.1128/MMBR.00078-15.
6. de Jong, M.F., and Alto, N.M. (2018). Cooperative Immune Suppression by *Escherichia coli* and Shigella Effector Proteins. Infect. Immun. *86*. https://doi.org/10.1128/IAI.00560-17.
7. Finlay, B.B., and McFadden, G. (2006). Anti-Immunology: Evasion of the Host Immune System by Bacterial and Viral Pathogens. Cell *124*, 767–782. https://doi.org/10.1016/j.cell.2006.01.034.
8. Hornef, M.W., Wick, M.J., Rhen, M., and Normark, S. (2002). Bacterial strategies for overcoming host innate and adaptive immune responses. Nat. Immunol. *3*, 1033–1040. https://doi.org/10.1038/ni1102-1033.
9. Martin, R.M., and Bachman, M.A. (2018). Colonization, Infection, and the Accessory Genome of *Klebsiella pneumoniae*. Front. Cell. Infect. Microbiol. *8*, 4. https://doi.org/10.3389/fcimb.2018.00004.
10. Opoku-Temeng, C., Malachowa, N., Kobayashi, S.D., and DeLeo, F.R. (2022). Innate Host Defense against *Klebsiella pneumoniae* and the Outlook for Development of Immunotherapies. J. Innate Immun. *14*, 167–181. https://doi.org/10.1159/000518679.
11. Cano, V., March, C., Insua, J.L., Aguiló, N., Llobet, E., Moranta, D., Regueiro, V., Brennan, G.P., Millán-Lou, M.I., Martín, C., et al. (2015). *Klebsiella pneumoniae* survives within macrophages by avoiding delivery to lysosomes. Cell *17*, 1537–1560. https://doi.org/10.1111/cmi.12466.
12. Lam, M.M.C., Wyres, K.L., Judd, L.M., Wick, R.R., Jenney, A., Brisse, S., and Holt, K.E. (2018). Tracking key virulence loci encoding aerobactin and salmochelin siderophore synthesis in *Klebsiella pneumoniae*. Genome Med. *10*, 77. https://doi.org/10.1186/s13073-018-0587-5.
13. Cortés, G., Borrell, N., de Astorza, B., Gómez, C., Sauleda, J., and Albertí, S. (2002). Molecular Analysis of the Contribution of the Capsular Polysaccharide and the Lipopolysaccharide O Side Chain to the Virulence of *Klebsiella pneumoniae* in a Murine Model of Pneumonia. Infect. Immun. *70*, 2583–2590. https://doi.org/10.1128/IAI.70.5.2583-2590.2002.
14. Muselius, B., Sukumaran, A., Yeung, J., and Geddes-McAlister, J. (2020). Iron limitation in *Klebsiella pneumoniae* defines new roles for Lon protease in homeostasis and degradation by quantitative proteomics. Front. Microbiol. *11*, 546.
15. Reitzel, C., Sukumaran, A., Muselius, B., O'Connor, S., and Geddes-McAlister, J. (2023). Profiling of the *Klebsiella pneumoniae* Phosphoproteome under Iron-Limited and Iron-Replete Conditions. Microbiol. Resour. Announc. *12*. https://doi.org/10.1128/mra.00186-23.
16. Reitzel, C., Sukumaran, A., Zanetti, C., Muselius, B., and Geddes-McAlister, J. (2023). Phosphoproteome Profiling of *Klebsiella pneumoniae* under Zinc-Limited and Zinc-Replete Conditions. Microbiol. Resour. Announc. *12*. https://doi.org/10.1128/mra.00258-23.
17. Sukumaran, A., Pladwig, S., and Geddes-McAlister, J. (2021). Zinc limitation in *Klebsiella pneumoniae* profiled by quantitative proteomics influences transcriptional regulation and cation transporter-associated capsule production. BMC Microbiol. *21*, 1–15. https://doi.org/10.1186/s12866-021-02091-8.
18. Sukumaran, A., Ball, B., Krieger, J.R., and Geddes-McAlister, J. (2022). Cross-Kingdom Infection of Macrophages Reveals Pathogen- and Immune-Specific Global Reprogramming and Adaptation. mBio *13*. https://doi.org/10.1128/mbio.01687-22.
19. Zambelloni, R., Marquez, R., and Roe, A.J. (2015). Development of antivirulence compounds: A biochemical review. Chem. Biol. Drug Des. *85*, 43–55. https://doi.org/10.1111/cbdd.12430.
20. DIckey, S.W., Cheung, G.Y.C., and Otto, M. (2017). Different drugs for bad bugs: Antivirulence strategies in the age of antibiotic resistance. Nat. Rev. Drug Discov. *16*, 457–471. https://doi.org/10.1038/nrd.2017.23.

21. Hennequin, C., and Robin, F. (2016). Correlation between antimicrobial resistance and virulence in *Klebsiella pneumoniae*. Eur. J. Clin. Microbiol. Infect. Dis. *35*, 333–341. https://doi.org/10.1007/s10096-015-2559-7.

22. Ernst, C.M., Braxton, J.R., Rodriguez-Osorio, C.A., Zagieboylo, A.P., Li, L., Pironti, A., Manson, A.L., Nair, A.V., Benson, M., Cummins, K., et al. (2020). Adaptive evolution of virulence and persistence in carbapenem-resistant *Klebsiella pneumoniae*. Nat. Med. *26*, 705–711. https://doi.org/10.1038/s41591-020-0825-4.

23. Dai, P., and Hu, D. (2022). The making of hypervirulent *Klebsiella pneumoniae*. J. Clin. Lab. Anal. *36*. https://doi.org/10.1002/jcla.24743.

24. Russo, T.A., and Marr, C.M. (2019). Hypervirulent *Klebsiella pneumoniae*. Clin. Microbiol. Rev. *32*. https://doi.org/10.1128/CMR.00001-19.

25. Choby, J.E., Howard-Anderson, J., and Weiss, D.S. (2020). Hypervirulent *Klebsiella pneumoniae* – clinical and molecular perspectives. J. Intern. Med. *287*, 283–300. https://doi.org/10.1111/joim.13007.

26. Ibrahim, S.F., and van den Engh, G. (2007). Flow Cytometry and Cell Sorting. Front. Med. (Lausanne), 19–39. https://doi.org/10.1007/10_2007_073.

27. Wyatt Shields Iv, C., Reyes, C.D., and López, G.P. (2015). Microfluidic cell sorting: A review of the advances in the separation of cells from debulking to rare cell isolation. Lab Chip *15*, 1230. https://doi.org/10.1039/c4lc01246a.

28. Dittrich, P.S., and Manz, A. (2006). Lab-on-a-chip: Microfluidics in drug discovery. Nat. Rev. Drug. Discov. *5*, 210. https://doi.org/10.1038/nrd1985.

29. Wu, Z., Willing, B., Bjerketorp, J., Jansson, J.K., and Hjort, K. (2009). Soft inertial microfluidics for high throughput separation of bacteria from human blood cells. Lab Chip *9*, 1193. https://doi.org/10.1039/b817611f.

30. Douglas, T.A., Cemazar, J., Balani, N., Sweeney, D.C., Schmelz, E.M., and Davalos, R.V. (2017). A feasibility study for enrichment of highly aggressive cancer subpopulations by their biophysical properties via dielectrophoresis enhanced with synergistic fluid flow. Electrophoresis *38*, 1507–1514. https://doi.org/10.1002/elps.201600530.

31. Čemažar, J., Douglas, T.A., Schmelz, E.M., and Davalos, R.V. (2016). Enhanced contactless dielectrophoresis enrichment and isolation platform via cell-scale microstructures. Biomicrofluidics *10*, 014109. https://doi.org/10.1063/1.4939947.

32. Rieckmann, J.C., Geiger, R., Hornburg, D., Wolf, T., Kveler, K., Jarrossay, D., Sallusto, F., Shen-Orr, S.S., Lanzavecchia, A., Mann, M., et al. (2017). Social network architecture of human immune cells unveiled by quantitative proteomics. Nat. Immunol. *18*, 583–593. https://doi.org/10.1038/ni.3693.

33. Aebersold, R., and Mann, M. (2016). Mass-spectrometric exploration of proteome structure and function. Nature *537*, 347–355. https://doi.org/10.1038/nature19949.

34. Sukumaran, A., Woroszchuk, E., Ross, T., and Geddes-McAlister, J. (2021). Proteomics of host–bacterial interactions: new insights from dual perspectives. Can. J. Microbiol. *67*, 213–225. https://doi.org/10.1139/cjm-2020-0324.

35. Sukumaran, A., Coish, J., Yeung, J., Muselius, B., Gadjeva, M., MacNeil, A., and Geddes-McAlister, J. (2019). Decoding communication patterns of the innate immune system by quantitative proteomics. J. Leukoc. Biol. *106*, 1221–1232.

36. Ball, B., Sukumaran, A., and Geddes-McAlister, J. (2020). Label-free quantitative proteomics workflow for discovery-driven host-pathogen interactions. JoVE J. https://doi.org/10.3791/61881.

37. Ball, B., Sukumaran, A., Krieger, J.R., and Geddes-McAlister, J. (2024). Comparative Cross-Kingdom DDA- and DIA-PASEF Proteomic Profiling Reveals Novel Determinants of Fungal Virulence and a Putative Druggable Target. J. Proteome Res. *23*, 3917–3932. https://doi.org/10.1021/acs.jproteome.4c00255.

38. Honeywell, E., Ball, B., Sukumaran, A., Muselius, B., Ströhle, G., Li, H., and Geddes-McAlister, J. (2026). The infection-exclusive proteome of murine extracellular vesicles defines *Klebsiella pneumoniae*-induced immune response signatures. Can. J. Microbiol. https://doi.org/10.1139/cjm-2025-0043.

39. Riley, M. (1999). Size Limits of Very Small Microorganisms: Proceedings of a Workshop (National Academies Press).

40. Cox, J., and Mann, M. (2012). 1D and 2D annotation enrichment: a statistical method integrating quantitative proteomics with complementary high-throughput data. BMC Bioinf. *13*, S12. https://doi.org/10.1186/1471-2105-13-S16-S12.

41. Janeway, C.A., and Medzhitov, R. (2002). Innate Immune Regulation. Annu. Rev. Immunol. https://doi.org/10.1146/annurev.immunol.20.083001.084359.

42. Eshleman, E.M., Delgado, C., Kearney, S.J., Friedman, R.S., and Lenz, L.L. (2017). Down regulation of macrophage IFNGR1 exacerbates systemic *L. monocytogenes* infection. PLoS Pathog. *13*, e1006388. https://doi.org/10.1371/journal.ppat.1006388.

43. Yin, F., Banerjee, R., Thomas, B., Zhou, P., Qian, L., Jia, T., Ma, X., Ma, Y., Iadecola, C., Beal, M.F., et al. (2010). Exaggerated inflammation, impaired host defense, and neuropathology in progranulin-deficient mice. J. Exp. Med. *207*, 117–128. https://doi.org/10.1084/jem.20091568.

44. Albertí, S., Marqués, G., Camprubí, S., Merino, S., Tomás, J.M., Vivanco, F., and Benedí, V.J. (1993). C1q binding and activation of the complement classical pathway by *Klebsiella pneumoniae* outer membrane proteins. Infect. Immun. *61*, 852–860. https://doi.org/10.1128/iai.61.3.852-860.1993.

45. Page, L.K., Staples, K.J., Spalluto, C.M., Watson, A., and Wilkinson, T.M.A. (2021). Influence of Hypoxia on the Epithelial-Pathogen Interactions in the Lung: Implications for Respiratory Disease. Front. Immunol. *12*. https://doi.org/10.3389/fimmu.2021.653969.

46. Hammond, F.R., Lewis, A., and Elks, P.M. (2020). If it's not one thing, HIF's another: immunoregulation by hypoxia inducible factors in disease. FEBS J. *287*, 3907–3916. https://doi.org/10.1111/febs.15476.

47. Petenkova, A., Auger, S.A., Lamb, J., Quellier, D., Carter, C., To, O.T., Milosevic, J., Barghout, R., Kugadas, A., Lu, X., et al. (2023). Prenylcysteine oxidase 1 like protein is required for neutrophil bactericidal activities. Nat. Commun. *14*, 2761. https://doi.org/10.1038/s41467-023-38447-z.

48. Shi, Y., Zhang, H., and Miao, C. (2025). Metabolic reprogram and T cell differentiation in inflammation: current evidence and future perspectives. Cell Death Discov. *11*, 123. https://doi.org/10.1038/s41420-025-02403-1.

49. Pearce, E.L., and Pearce, E.J. (2013). Metabolic Pathways in Immune Cell Activation and Quiescence. Immunity *38*, 633–643. https://doi.org/10.1016/j.immuni.2013.04.005.

50. Ganeshan, K., and Chawla, A. (2014). Metabolic Regulation of Immune Responses. Annu. Rev. Immunol. *32*, 609–634. https://doi.org/10.1146/annurev-immunol-032713-120236.

51. Fontenot, C.R., Tasnim, H., Valdes, K.A., Popescu, C.V., and Ding, H. (2020). Ferric uptake regulator (Fur) reversibly binds a [2Fe-2S] cluster to sense intracellular iron homeostasis in *Escherichia coli*. J. Biol. Chem. *295*, 15454–15463. https://doi.org/10.1074/jbc.RA120.014814.

52. Mey, A.R., Gómez-Garzón, C., and Payne, S.M. (2021). Iron Transport and Metabolism in *Escherichia*, *Shigella*, and *Salmonella*. EcoSal Plus *9*, eESP00342020. https://doi.org/10.1128/ecosalplus.ESP-0034-2020.

53. Maunders, E.A., Ganio, K., Hayes, A.J., Neville, S.L., Davies, M.R., Strugnell, R.A., McDevitt, C.A., and Tan, A. (2022). The Role of ZntA in *Klebsiella pneumoniae* Zinc Homeostasis. Microbiol. Spectr. *10*. https://doi.org/10.1128/spectrum.01773-21.

54. Outten, C.E., and O'Halloran, T.V. (2001). Femtomolar Sensitivity of Metalloregulatory Proteins Controlling Zinc Homeostasis. Science *292*, 2488–2492. https://doi.org/10.1126/science.1060331.

55. Abdul-Tehrani, H., Hudson, A.J., Chang, Y.-S., Timms, A.R., Hawkins, C., Williams, J.M., Harrison, P.M., Guest, J.R., and Andrews, S.C. (1999). Ferritin Mutants of *Escherichia coli* Are Iron Deficient and Growth Impaired, and *fur* Mutants are Iron Deficient. J. Bacteriol. *181*, 1415–1428. https://doi.org/10.1128/JB.181.5.1415-1428.1999.

56. Hood, M.I., and Skaar, E.P. (2012). Nutritional immunity: transition metals at the pathogen–host interface. Nat. Rev. Microbiol. *10*, 525–537. https://doi.org/10.1038/nrmicro2836.

57. Engelsöy, U., Rangel, I., and Demirel, I. (2019). Impact of Proinflammatory Cytokines on the Virulence of Uropathogenic *Escherichia coli*. Front. Microbiol. *10*. https://doi.org/10.3389/fmicb.2019.01051.

58. Chen, S., Saeed, A.F.U.H., Liu, Q., Jiang, Q., Xu, H., Xiao, G.G., Rao, L., and Duo, Y. (2023). Macrophages in immunoregulation and therapeutics. Signal Transduct. Targeted Ther. *8*, 207. https://doi.org/10.1038/s41392-023-01452-1.

59. Simões, R.L., Arruda, M.A., Canetti, C., Serezani, C.H., Fierro, I.M., and Barja-Fidalgo, C. (2013). Proinflammatory Responses of Heme in Alveolar Macrophages: Repercussion in Lung Hemorrhagic Episodes. Mediat. Inflamm. *2013*, 1–11. https://doi.org/10.1155/2013/946878.

60. Nowak, J.E., Harmon, K., Caldwell, C.C., and Wong, H.R. (2012). Prophylactic zinc supplementation reduces bacterial load and improves survival in a murine model of sepsis. Pediatr. Crit. Care Med. *13*, e323–e329. https://doi.org/10.1097/PCC.0b013e31824fbd90.

61. Stafford, S.L., Bokil, N.J., Achard, M.E.S., Kapetanovic, R., Schembri, M.A., McEwan, A.G., and Sweet, M.J. (2013). Metal ions in macrophage antimicrobial pathways: emerging roles for zinc and copper. Biosci. Rep. *33*. https://doi.org/10.1042/BSR20130014.

62. Lopez, C.A., and Skaar, E.P. (2018). The Impact of Dietary Transition Metals on Host-Bacterial Interactions. Cell Host Microbe *23*, 737–748. https://doi.org/10.1016/j.chom.2018.05.008.

63. Kelley, V.A., and Schorey, J.S. (2003). *Mycobacterium* 's Arrest of Phagosome Maturation in Macrophages Requires Rab5 Activity and Accessibility to Iron. Mol. Biol. Cell *14*, 3366–3377. https://doi.org/10.1091/mbc.e02-12-0780.

64. Nagy, T.A., Moreland, S.M., and Detweiler, C.S. (2014). *Salmonella* acquires ferrous iron from haemophagocytic macrophages. Mol. Microbiol. *93*, 1314–1326. https://doi.org/10.1111/mmi.12739.

65. Mitchell*, G., Chen*, C., and Portnoy, D.A. (2016). Strategies Used by Bacteria to Grow in Macrophages. Microbiol. Spectr. *4*. https://doi.org/10.1128/microbiolspec.MCHD-0012-2015.

66. Kaufmann, S.H.E., and Dorhoi, A. (2016). Molecular Determinants in Phagocyte-Bacteria Interactions. Immunity *44*, 476–491. https://doi.org/10.1016/j.immuni.2016.02.014.

67. Weiss, G., Ganz, T., and Goodnough, L.T. (2019). Anemia of inflammation. Blood *133*, 40–50. https://doi.org/10.1182/blood-2018-06-856500.

68. Forbes, J.R., and Gros, P. (2001). Divalent-metal transport by NRAMP proteins at the interface of host–pathogen interactions. Trends Microbiol. *9*, 397–403. https://doi.org/10.1016/S0966-842X(01)02098-4.

69. Zierke, L., Mourad, R., Kohler, T.P., Müsken, M., and Hammerschmidt, S. (2025). Influence of the polysaccharide capsule on virulence and fitness of *Klebsiella pneumoniae*. Front. Microbiol. *16*. https://doi.org/10.3389/fmicb.2025.1450984.

70. Chu, W.H.W., Tan, Y.H., Tan, S.Y., Chen, Y., Yong, M., Lye, D.C., Kalimuddin, S., Archuleta, S., and Gan, Y.-H. (2023). Acquisition of regulator on virulence plasmid of hypervirulent *Klebsiella* allows bacterial lifestyle switch in response to iron. mBio. https://doi.org/10.1128/mbio.01297-23.

71. Yang, Y., Batista, M., Clarke, B.R., Agyare-Tabbi, M.R., Song, H., Kuehfuss, N.M., Le Bas, A., Robinson, C.V., Whitfield, C., Stansfeld, P.J., et al. (2025). Molecular basis for the phosphorylation of bacterial tyrosine kinase Wzc. Nat. Commun. *16*, 3437. https://doi.org/10.1038/s41467-025-58693-7.

72. Needham, B.D., and Trent, M.S. (2013). Fortifying the barrier: the impact of lipid A remodelling on bacterial pathogenesis. Nat. Rev. Microbiol. *11*, 467–481. https://doi.org/10.1038/nrmicro3047.

73. Keenan, J.I., Davis, K.A., Beaugie, C.R., McGovern, J.J., and Moran, A.P. (2008). Alterations in *Helicobacter pylori* outer membrane and outer membrane vesicle-associated lipopolysaccharides under iron-limiting growth conditions. Innate Immun. *14*, 279–290. https://doi.org/10.1177/1753425908096857.

74. Reynolds, C.M., Kalb, S.R., Cotter, R.J., and Raetz, C.R.H. (2005). A Phosphoethanolamine Transferase Specific for the Outer 3-Deoxy-D-manno-octulosonic Acid Residue of *Escherichia coli* Lipopolysaccharide. J. Biol. Chem. *280*, 21202–21211. https://doi.org/10.1074/jbc.M500964200.

75. Cellier, M.F., Courville, P., and Campion, C. (2007). Nramp1 phagocyte intracellular metal withdrawal defense. Microb. Infect. *9*, 1662–1670. https://doi.org/10.1016/j.micinf.2007.09.006.

76. Prudhomme, Pastora, R., Mclean, M.D., Cossar, D., and Geddes-McAlister, J. (2021). Exposure of *Agrobacterium tumefaciens* to agroinfiltration medium demonstrates cellular remodeling and may promote enhanced adaptability for molecular pharming. Can. J. Microbiol. https://doi.org/10.1139/cjm-2020-0239.

77. Prudhomme, Gianetto-Hill, C., Pastora, R., Cheung, W.-F., Allen-Vercoe, E., McLean, M.D., Cossar, D., and Geddes-McAlister, J. (2021). Quantitative proteomic profiling of shake flask versus bioreactor growth reveals distinct responses of *Agrobacterium tumefaciens* for preparation in molecular pharming. Can. J. Microbiol. *67*, 75–84. https://doi.org/10.1139/cjm-2020-0238.

78. Prudhomme, N., Pastora, R., Thomson, S., Zheng, E., Sproule, A., Krieger, J.R., Murphy, J.P., Overy, D.P., Cossar, D., McLean, M.D., et al. (2024). Bacterial growth-mediated systems remodelling of *Nicotiana benthamiana* defines unique signatures of target protein production in molecular pharming. Plant Biotechnol. J. *22*, 2248–2266. https://doi.org/10.1111/pbi.14342.

79. Rostam, H.M., Singh, S., Salazar, F., Magennis, P., Hook, A., Singh, T., Vrana, N.E., Alexander, M.R., and Ghaemmaghami, A.M. (2016). The impact of surface chemistry modification on macrophage polarisation. Immunobiology *221*, 1237–1246. https://doi.org/10.1016/j.imbio.2016.06.010.

80. Petty, H.R., Hafeman, D.G., and McConnell, H.M. (1981). Disappearance of macrophage surface folds after antibody-dependent phagocytosis. J. Cell Biol. *89*, 223–229. https://doi.org/10.1083/jcb.89.2.223.

81. Liu, X., Xu, Q., Yang, X., Heng, H., Yang, C., Yang, G., Peng, M., Chan, E.W.-C., and Chen, S. (2025). Capsular polysaccharide enables *Klebsiella pneumoniae* to evade phagocytosis by blocking host-bacteria interactions. mBio *16*, e0383824. https://doi.org/10.1128/mbio.03838-24.

82. Vo, L., Avgidis, F., Mattingly, H.H., Edmonds, K., Burger, I., Balasubramanian, R., Shimizu, T.S., Kazmierczak, B.I., and Emonet, T. (2025). Nongenetic adaptation by collective migration. Proc. Natl. Acad. Sci. USA *122*, e2423774122. https://doi.org/10.1073/pnas.2423774122.

83. Raub, C.B., Suresh, V., Krasieva, T., Lyubovitsky, J., Mih, J.D., Putnam, A.J., Tromberg, B.J., and George, S.C. (2007). Noninvasive Assessment of Collagen Gel Microstructure and Mechanics Using Multiphoton Microscopy. Biophys. J. *92*, 2212–2222. https://doi.org/10.1529/biophysj.106.097998.

84. Wiśniewski, J.R., Zougman, A., Nagaraj, N., and Mann, M. (2009). Universal sample preparation method for proteome analysis. Nat. Methods *6*, 359. https://doi.org/10.1038/nmeth.1322.

85. Rappsilber, J., Mann, M., and Ishihama, Y. (2007). Protocol for micro-purification, enrichment, pre-fractionation and storage of peptides for proteomics using StageTips. Nat. Protoc. *2*, 1896–1906. https://doi.org/10.1038/nprot.2007.261.

86. Cox, J., and Mann, M. (2008). MaxQuant enables high peptide identification rates, individualized p.p.b.-range mass accuracies and proteome-wide protein quantification. Nat. Biotechnol. *26*, 1367–1372. https://doi.org/10.1038/nbt.1511.

87. Cox, J., Neuhauser, N., Michalski, A., Scheltema, R.A., Olsen, J.V., and Mann, M. (2011). Andromeda: A peptide search engine integrated into the MaxQuant environment. J. Proteome Res. *10*, 1794–1805. https://doi.org/10.1021/pr101065j.

88. Tyanova, S., Temu, T., Sinitcyn, P., Carlson, A., Hein, M.Y., Geiger, T., Mann, M., and Cox, J. (2016). The Perseus computational platform for comprehensive analysis of (prote) omics data. Nat. Methods *13*, 731–740.

89. Benjamini, Y., and Hochberg, Y. (1995). Controlling the False Discovery Rate: A Practical and Powerful Approach to Multiple Testing. J. Roy. Stat. Soc. B *57*, 289–300. https://doi.org/10.1111/j.2517-6161.1995.tb02031.x.

90. Ashburner, M., Ball, C.A., Blake, J.A., Botstein, D., Butler, H., Cherry, J.M., Davis, A.P., Dolinski, K., Dwight, S.S., Eppig, J.T., et al. (2000). Gene Ontology: tool for the unification of biology. Nat. Genet. *25*, 25–29. https://doi.org/10.1038/75556.

91. Olabisi-Adeniyi, E., McAlister, J.A., Ferretti, D., Cox, J., and Geddes-McAlister, J. (2025). ProteoPlotter: an executable proteomics visualization tool compatible with Perseus. J. Proteome Res. https://doi.org/10.1101/2024.12.30.630796.

STAR★METHODS

KEY RESOURCES TABLE

REAGENT or RESOURCE	SOURCE	IDENTIFIER
Bacterial and virus strains		
YFP-tagged *Escherichia coli* induced with plasmid HCB33/pVS133	Shimizu lab - AMOLF	N/A
Klebsiella pneumoniae wild-type (K52 serotype)	Geddes-McAlister lab	N/A
Chemicals, peptides, and recombinant proteins		
SU-8 3005 photoresist	MicroChem Corp	Cat Y311049
SU8 developer (MR-DEV 600)	micro resist technology GmbH	Cat R815100
isopropanol	Sigma-Aldrich	Cat W292907
SU-8 3025 photoresist	MicroChem Corp	Cat Y311072
EBR PG chemical	MicroChem Corp	Cat G042075
trichloro(1H,1H,2H,2H-perfluorooctyl)-silane	Sigma-Aldrich	Cat 448931
PDMS & curing agent (DC Sylgard 184 elastomer kit, 1.1kg)	Mavom BV	Cat 1060040_S1,1K
Pluronic® F108	Sigma-Aldrich	Cat 542342
phosphate-buffered saline	Sigma-Aldrich	Cat P4474
Gibco® Dulbecco's Modified Eagle Medium	Thermo Fisher Scientific	Cat 41965039
fetal bovine serum	Thermo Fisher Scientific	Cat A3840402
glutaMAX	Thermo Fisher Scientific	Cat 35050061
sodium pyruvate	Capricorn Scientific	Cat NPY-B
L-glutamine	Lonza	Cat BEBP17-605E
Penicillin-Streptomycin	Westburg	Cat CA PS-B
Trypsin-EDTA (0.25%) with phenol red	VWR International BV	Cat 392-0435
Tryptone Broth	VWR International BV	J870
ampicillin	Sigma-Aldrich	Cat A9393
isopropyl β-*d*-1-thiogalactopyranoside	Sigma-Aldrich	Cat I6758
poly-L-lysine	Sigma Aldrich	Cat P8920
Tryptic Soy Broth	Fluka Analytical	Cat T8907
Luria Bertani (LB) agar plates	Thermo Fisher Scientific	Cat A55800
proteinase inhibitor cocktail tablet	Sigma-Aldrich	Cat 11697498001
sodium dodecyl sulfate	Thermo Fisher Scientific	Cat J18220.36
dithiothreitol	Sigma-Aldrich	Cat 10197777001
iodoacetamide	Sigma-Aldrich	Cat I1149
urea	Sigma-Aldrich	Cat U5378
HEPES	Sigma-Aldrich	Cat H23830
acetone	Sigma-Aldrich	Cat 179124
trypsin/Lys-C	Promega	Cat V5071
acetonitrile	Sigma-Aldrich	Cat 34851
acetic acid	Sigma-Aldrich	Cat 5.33001
formic acid	Sigma-Aldrich	Cat 900687
Experimental models: Organisms/strains		
mouse: immortalized BALB/c wild-type macrophages	Geddes-McAlister lab	N/A
Software and algorithms		
Fiji	NIH	https://imagej.net/Fiji/Download
MATLAB2022b	Mathworks	https://www.mathworks.com/products/matlab.html
CleWin3	WieWeb	https://wieweb.com/site/downloads/
GraphPad Prism 10	GraphPad	https://www.graphpad.com/
Code for automated counting of E. coli	Vo, Lam et al.[68]	N/A

EXPERIMENTAL MODEL AND STUDY PARTICIPANT DETAILS

Macrophage cell culture

Immortalized murine BALB/c macrophage derived from 7-to-10-week-old female mice (generously provided by Dr. Felix Meissner, University Hospital Bonn) were grown in a T-25 flask (Corning, tissue-culture-treated surface, Sigma-Aldrich) containing antibiotic supplemented Dulbecco's Modified Eagle Medium (DMEM; Gibco, Thermo Fisher Scientific) medium with 10% fetal bovine serum (FBS, Thermo Fisher Scientific), 2 mM Glutamax (Thermo Fisher Scientific), 1% sodium pyruvate (Capricorn Scientific), 1% L-glutamine, and 5% Pen-Strep (Penicillin-Streptomycin, Westburg) (Sigma-Aldrich) at 37°C with 5% CO_2. The cells were passaged two times per week (upon reaching 70–80% confluence) by releasing from the surface using a cell scraper or Trypsin-EDTA (0.25%) with phenol red (VWR International BV). Additionally, cells were counted using LUNA-II Automated Cell Counter or a hemocytometer and the experiment was performed with passage number between 5 and 20. Notably, for iron utilization assays, three biological replicates of supernatant from macrophage (uninfected) were collected and filtered with 0.2 μm pore membrane under sterile conditions prior to *K. pneumoniae* exposure.

Bacterial strain preparation

For microfluidic chip testing, non-pathogenic *Escherichia coli* transformed with an inducible plasmid, HCB33/pVS133, expressing yellow fluorescent protein (YFP) (obtained from Shimizu lab at AMOLF) was used. Briefly, YFP-*E. coli* cells were grown in Tryptone Broth (TB; VWR International BV) medium supplemented with ampicillin (100 mg/L, Sigma-Aldrich) overnight (12–14 h, at 30°C). The overnight bacteria were sub-cultured at 1:100 dilution in TB medium supplemented with ampicillin (100 mg/L) and isopropyl β-*d*-1-thiogalactopyranoside (IPTG, 100 μM; Sigma-Aldrich) for 4 h at 33.5°C prior to the experiment. Next, 3 mL of YFP-*E. coli* in 0.01 M PBS (optical density ∼0.1; 10^8 cells/mL) was processed inside the 1.4 μm filter-height chip at 6 mL/h flow rate and observed using the confocal microscope (Nikon A1R-MP).

Additionally, to test the performance of the chip in separating macrophage and bacterial cells based on their sizes and shapes, a 3 mL mixture containing macrophage (∼1.5×10^6 cells/mL) and YFP-*E. coli* (∼10^8 cells/mL) in PBS was pumped directly through the chip (without incubation) at 6 mL/h. The samples collected from the main (∼1 mL) and side (∼2 mL) outlets were observed under a microscope (Nikon A1R-MP) with coverslip (Menzel-Glaser, 24 × 24 mm # 1, Thermo Scientific) pre-coated with poly-L-lysine (PLL, Sigma-Aldrich) 0.1% (w/v). YFP-*E. coli* and macrophages were detected at excitation/emission 488/520–550 nm and brightfield mode, respectively. Cells were counted manually or automatically (for fluorescent YFP-*E. coli*) using image analysis code adapted from[82] a modified Otsu algorithm for segmentation. The proportion (%) of the collected cells was calculated from the cell ratio between the main and side outlet sample. The experiment was performed in three biological replicates. Data was plotted and analyzed using GraphPad Prism 10.

Following microfluidic chip testing with *E. coli* (Biosafety level 1; AMOLF), we prepared the full experiment using *K. pneumoniae* (Biosafety level 2; University of Guelph). Notably, comparable size and shape between *E. coli* (i.e., 1.0–2.0 μm long, 1.0 μm diameter, straight rod shape) and *K. pneumoniae* (0.6–6.0 μm long, 0.3–1.0 μm diameter, straight rod shape) enabled translation of optimal chip heights between experiments. *K. pneumoniae* subsp. *pneumoniae* wild-type (Kp52.145) strain was maintained on Tryptic Soy Broth (TSB) (Fluka Analytical) or Luria Bertani (LB) agar plates (Thermo Fisher Scientific) and grown overnight at 37°C in TSB or LB media followed by sub-culturing in TSB or LB to mid-log phase.

Co-culturing for macrophage and *K. pneumoniae*

BALB/c macrophages were grown to 70–80% confluence in a 10 cm cell culture-treated dish (Thermo Scientific) in DMEM containing 10% FBS, 2 mM Glutamax, 1% sodium pyruvate, 1% L-glutamine and 5% Pen-Strep at 37°C with 5% CO_2. *K. pneumoniae* were grown in TSB to mid-log phase, collected, washed with PBS, counted with a hemocytometer and resuspended in DMEM containing 10% FBS and 1% L-glutamine to 10^8 cells/mL. A multiplicity of infection (MOI) of 100:1 (bacteria:macrophage) was established followed by a 90 min incubation at 37°C with 5% CO_2. Four biological and two experimental replicates were performed. Notably, for iron utilization assays, three biological replicates of supernatant from macrophage co-cultured with *K. pneumoniae* was collected and filtered with 0.2 μm under sterile conditions prior to *K. pneumoniae* exposure. We also performed colony forming unit counts to ensure phagocytosis of the *K. pneumoniae* Kp52.145 strain by macrophage following MOI 100:1 and 90 min co-culture. Macrophage were lysed with sterile dH_2O, followed by serial dilutions and plating of dilutions on TSB at 30°C for 24 h prior to enumerating colonies.

METHOD DETAILS

Microfluidic chip design

The chip microstructure was redrawn using CleWin3 software based on a previous design.[83] The chip consisted of an inlet, leading to four similar separators arranged in parallel with one main channel and two series of crossflow filter channels (Figure S10, chip design files available from the authors upon request). A range of filter heights (i.e., 1.4, 3.5, and 4.5 μm) were tested for collection of designated cell types (i.e., macrophage vs. bacteria). The designs were printed on the negative masks (material: 5″ × 5″ x 0.090″ quartz; address size (μ): 0.0625; minimum feature size (μ): 2.0; CD tolerance ±(μ): 0.25; defect density (μ): <1psi@1.0) with the designed features being transparent on the masks and the chrome side facing down (Compugraphics, UK).

Master mold fabrication with photolithography

Master molds for 1.4, 3.5, and 4.5 μm filter-height chips were fabricated on a silicon wafer (University Wafers) using two-layer photolithographic steps: the first layer contained filter channels; the second layer contained side channels, main channel, inlet, and outlets (Figure S11). Briefly, for the filter channel layer, SU-8 3001 photoresist (1:1 of SU-8 3005: MicroChem Corp; cyclopentanone) was spun on the wafer (Suss Delta 80 Spin coater) at the speed of 3,000 rpm for 40 s to reach the thickness of 1.4 μm. The wafer was then soft-baked at 95°C for 3 min, exposed to ultraviolet (UV) light through the photomask for 10 s (Suss MABA6 Mask aligner), hard-baked at 95°C for 3 min, developed twice with SU8 developer (microresist mr-Dev 600 [MR-DEV 600], micro resist technology GmbH) and cleaned twice with isopropanol (IPA; Sigma-Aldrich). For the layer containing the side channels, main channel, inlet, and outlets, SU-8 3025 (MicroChem Corp) was spun at the speed of 1,750 rpm for 30 s to reach the thickness of about 40 μm on the same wafer that contained the filter layer. After that, the wafer was soft baked at 65°C for 3 min, then at 95°C for 7 min. For aligning the channel layer with the filter layer at a high resolution before the UV exposure, an edge bead removing step was done by dropping EBR PG chemical (MicroChem Corp) slowly at the edge of the wafer while spinning at 300 rpm to remove the thick photoresist building up at that region and make the aligning markers visible. The wafer was subsequently baked at 95°C for 3 min. As soon as the channel layer had been well aligned above the filter layer using the markers, the UV light was exposed through the photomask for 11 s and the wafer was hard-baked at 65°C for 3 min, then at 95°C for 7 min, and cleaned twice with MR-DEV 600 and IPA. Eventually, the wafer was hard-baked at 150°C for 1 h to remove cracks in the corners, then silanized with trichloro(1H,1H,2H,2H-perfluorooctyl)-silane (Sigma-Aldrich) under the vacuum oven at 50°C for 30 min and rinsed briefly again with IPA and Milli-Q water before use. The chip microstructure was observed using an optical microscopy (Zeiss Axioskop 2 MAT) and the heights of both layers were measured using a surface profiler (KLA-Tencor alpha-step 500) (Figure S5). All fabrication steps were conducted in the cleanroom facilities at AMOLF NanoLab Amsterdam.

PDMS chip fabrication

The polydimethylsiloxane (PDMS) microfluidic chip was fabricated by pouring 10:1 PDMS: curing agent (Mavom Chemical Solutions DC Sylgard 184 elastomer kit) onto the premade wafer, degassed, and cured at 80°C for at least 2 h. The PDMS chip was then cooled to room temperature, cut and peeled off from the wafer. Access holes to the inlet and outlets were punched (Reusable Biopsy Punch, 0.75 mm w/plunge), and the chip was bonded to a coverslip (Menzel- 6 Glaser, 24 × 60 mm # 1.5, Thermo Scientific) at 80°C for 10 min after a 1 min of activation with oxygen plasma using a plasma cleaner (PDC-002-HPCE, Harrick Plasma) equipped with a vacuum gauge (PDC-VCG-2, Harrick Plasma) and a vacuum pump (Dekker Vacuum Technologies). The inlet of the chip was connected to a stainless-steel PDMS coupler (inner diameter [ID] x outer diameter [OD] = 0.584 mm × 0.89 mm, L = 15 mm, gauge size = 20G, Darwin Microfluidics) connected to a biocompatible Tygon ND 100-80 tubing (ID x OD = 0.76 mm × 2.29 mm, L = 20 cm, Darwin Microfluidics). The other end of the inlet tube was connected to a blunt end luer lock syringe needle (ID x OD = 0.62 mm × 0.90 mm, gauge size = 20G, Darwin microfluidics) attached to a 10 mL disposable syringe (Terumo). The liquid sample was injected into the chip using a syringe pump (PSNE4000 Two channel syringe pump, ProSense). All outlets were connected directly with the Tygon ND 100-80 tubes (ID x OD = 0.76 mm × 2.29 mm, L = 2 cm, Darwin Microfluidics) with main and side channel outputs collected separately.

Pre-operation and testing of microfluidic chips

Prior to all chip experiments, 0.85 mg/mL Pluronic F108 (Sigma-Aldrich) in 0.01 M PBS (phosphate-buffered saline; Sigma-Aldrich) was prefilled in the chip using the syringe pump at 20 mL/h flow rate until chip was filled and no air bubbles were present. The chip was incubated for 15–30 min at room temperature in 0.01 M PBS to maintain a high moisture condition and flushed with 1 mL of 0.01 M PBS (at the rate of 20 mL/h) by the syringe pump. To test filter channel heights (i.e., 1.4, 3.5 and 4.5 μm) for cell separation, 3 mL of macrophage cells (immortalized cell line derived from BALB/c mice, obtained from Geddes-McAlister lab) in 0.01 M PBS ($\sim 1.5 \times 10^6$ cells/mL) was processed in each chip at 6 mL/h flow rate and observed with a microscope (ZEISS Axio Vert.A1). Experiment was performed in three biological replicates. Data was plotted and analyzed using GraphPad Prism 10.

Sample collection

Proteomic assessment was performed on samples collected from six conditions: *K. pneumoniae* only (bacterial cells in DMEM prior to co-culture), macrophage only (prior to co-culture), supernatant (supernatant of co-culture plates), scraping (cells of co-culture plates), main channel (chip-based separation through main channel), and side channel (chip-based separation through side channel) (Figure S12). The samples for traditional and chip-based separation were collected from the same experiment (i.e., same time, growth conditions, macrophage passage, bacterial inoculum). For *K. pneumoniae* only, 1 mL of bacterial cells were collected by centrifugation at 3,500 rcf, 20°C for 5 min, supernatant was removed, washed once with 0.01 M PBS, and flash frozen in liquid nitrogen prior to storage at −80°C. For macrophage only samples, following 90 min incubation with PBS, cell scraping was performed, macrophages were collected by centrifugation at 400 xg, 20°C for 5 min, washed once with 0.01 M PBS and frozen in liquid nitrogen prior to storage at −80°C. For supernatant samples (traditional technique), after 90 min co-culture with macrophage and *K. pneumoniae*, supernatant was collected by pipette and centrifuged at 3,500 xg, 20°C for 5 min, washed once with 0.01 M PBS and frozen in liquid nitrogen prior to storage at −80°C. For cell scraping samples (traditional technique), removal of the supernatant (outlined above), 10 mL of 0.01 M PBS was added to the plate, cells were released from the dish with a cell scraper (Corning), collected, and centrifuged at 400 xg, 20°C

for 5 min. The cell pellet was washed once with 0.01 M PBS and frozen in liquid nitrogen prior to storage at −80°C. For chip-based analysis, after 90 min co-culture with macrophage and *K. pneumoniae*, cells were resuspended in the supernatant with a cell scraper (Corning), collected in a single 15 mL Eppendorf tube, and processed through the microfluidic chip at 6 mL/h flow rate, 20°C for 50 min by the syringe pump system. The side-channel sample was collected by centrifugation at 3,500 xg, 20°C for 5 min; the cell pellet was washed once in 0.01 M PBS and frozen in liquid nitrogen prior to storage at −80°C. The main channel sample was collected by centrifugation at 400 xg, 20°C for 5 min and frozen in liquid nitrogen prior to storage at −80°C. Experiments were performed in four biological and two experimental replicates.

Sample preparation for proteomic profiling

The frozen cell pellets were prepared as previously described.[36] Briefly, cell pellets were resuspended in 300 μL cold 100 mM Tris-HCl at pH 8.5 containing a proteinase inhibitor cocktail tablet (Sigma-Aldrich) and 2% sodium dodecyl sulfate (SDS; Thermo Fisher Scientific). Samples were probe sonicated in an ice bath for 5 cycles (30 s on/30 s off), incubated with 10 mM dithiothreitol (DTT; Sigma-Aldrich) at 95°C for 10 min and 800 rpm agitation, followed by cooling and the addition of 55 mM iodoacetamide (IAA; Sigma-Aldrich) in the dark at room temperature for 20 min. Proteins were precipitated in 100% acetone overnight at −20°C followed by washing in 80% acetone (Sigma-Aldrich), resuspension in 8 M urea/40 mM HEPES (Sigma-Aldrich) and quantification using a tryptophan assay.[84] Proteins were normalized for trypsin/Lys-C (Promega) digestion (50:1, protein:enzyme) at room temperature overnight followed by peptide purification using C18 Stop And Go Extraction (STAGE) tips.[85]

Mass spectrometry

Peptides were resuspended in buffer A (0.1% formic acid, Sigma-Aldrich), separated by an Easy-nLC 1200 high-performance liquid chromatography device (75 μm × 50 cm PepMap inline RELC Easy-Spray C18 column; Thermo Fisher Scientific), and analyzed on an Orbitrap Exploris 240 hybrid quadrupole-orbitrap mass spectrometer (Thermo Fisher Scientific). Peptides were subjected to electrospray ionization into the mass spectrometer with a linear gradient of 3–20% buffer B (80% acetonitrile, 0.5% acetic acid) over a 3-h gradient, followed by a 100% buffer B wash at 250 nL/min flow rate. The mass spectrometer switched between one full scan and MS/MS scans on abundant peaks with full scans acquired (*m/z* 400 to 2000) at a resolution of 120,000 at 200 *m/z*.

Data processing and bioinformatics

Raw mass spectrometry data was processed using MaxQuant (v1.6.0.26, v2.4.0.0)[86] with a minimum of two unique peptides, trypsin enzyme specificity with two missed cleavages, fixed (i.e., carbamidomethylation) and variable (i.e., methionine oxidation and N-acetylation) modifications, false discovery rate (FDR) at 1%, label-free quantification (ratio of 1), match between runs enabled, and split by taxonomy ID. FASTA files from UniProt for *K. pneumoniae* K52 serotype (5,126 sequences; May 21, 2020) and *M. musculus* (55,462 sequences, June 1, 2020) were searched with Andromeda.[87] The output files were processed in Perseus (v1.6.2.2, v2.0.7.0)[88] with filtering for reverse database matches, contaminants, and proteins identified by site, $\log_2$ transformed LFQ intensities, filtering for valid values (i.e., proteins present in 3 of 4 replicates), and imputation from the normal distribution (width 0.3; downshift 1.8). Significant differences by Student's *t* test with multiple hypothesis testing correction[89] FDR at 0.05 and $S_0 = 1$. One-dimensional (1D) analysis was performed using a Student's *t* test with FDR = 0.05 and $S_0 = 1$ generating a "score" value that represents the relative intensities of proteins identified within a category where 1 indicates a significant enrichment and −1 indicates a significant depletion.[40] Proteins were categorized using Gene Ontology (GO) terms.[90] STRING networking mapping for protein-protein interactions was used (https://string-db.org). Visualization was performed using Perseus, ProteoPlotter,[91] and GraphPad Prism (v. 10).

Iron quantification assay

For *K. pneumoniae* exposure to macrophage supernatant (i.e., uninfected macrophage vs. macrophage co-cultured with *K. pneumoniae*), from overnight culture, 10^9 of *K. pneumoniae* cells were pelleted at 5,000 xg for 10 min at 4°C in biological triplicate and technical triplicate and washed twice with 1 mL sterile 0.01 M PBS. Cells were reconstituted in 200 μL DMEM and added to 2 mL filter-purified DMEM, uninfected macrophage supernatant, or *K. pneumoniae*-infected macrophage supernatant and incubated at 37°C for 2 h with 200 rpm shaking. For *K. pneumoniae* exposure to M9 minimal media, *K. pneumoniae* was sub-cultured 1/100 from overnight LB culture into 5 mL M9 media or M9 media supplemented with 10 μM $Fe_2(SO_4)_3$ in biological triplicate and technical duplicate.[14] Minimal media was made using Difco M9 Minimal salts containing 6.78 g/L Na_2HPO_4, 3 g/L KH_2PO_4, 0.5 g/L NaCl, 1 g/L NH_4Cl. Glucose was added to a final concentration of 0.4% (w/v) as well as 2 mM $MgSO_4$ and 0.1 mM $CaCl_2$. All solutions for minimal media were made using Chelex 100-treated (Bio-Rad) MilliQ water and glassware was rinsed with 3 M HCl to remove traces of iron. Sub-cultured cells were allowed to grow to mid-log phase for 5 h at 37°C with 200 rpm shaking. Cells were collected by centrifugation at 5,000 xg for 10 min at 4°C, washed twice with 5 mL 0.01 M PBS followed by 0.4 mL of 0.9% NaCl. Pellets were reconstituted with 200 μL lysis buffer (Thermo Cell Total Iron Colorimetric Kit, EEA009), vortexed, incubated on ice for 10 min and pelleted at 15,000 rcf for 10 min at 4°C. Supernatant was collected and 80 μL was added to a clear, 96 well plate with 80 μL chromogenic solution. The plate was incubated at 37°C for 40 min and absorbance was measured at optical density (OD) = 593 nm. As ferric iron (Fe^{3+}) is converted into ferrous iron (Fe^{2+}) during this process, total iron content is determined by comparing sample OD_{593nm} values to a standard curve of 0–50 μmol Fe/L generated using iron standard provided in kit. Data was plotted and analyzed using GraphPad Prism 10.

Macrophage infection with K. pneumoniae *grown in iron-limited and -supplemented media*

Macrophage cells were seeded in 12-well plates and grown to confluence as described above. DMEM media was removed, cells were washed twice with 1 mL room temperature 0.01 M PBS, then 5×10^7 *K. pneumoniae* in M9 minimal media or M9 minimal media supplemented with 10 μM $Fe_2(SO_4)_3$ were diluted in DMEM and added to macrophages in biological triplicate and technical duplicate. Additionally, three replicates of uninfected macrophages were grown in 1 mL DMEM without antibiotics. Cells were incubated at 37°C and 5% CO_2 for 90 min.

Lactate dehydrogenase cytotoxicity assay

Following *K. pneumoniae* and macrophage co-culture, cytotoxicity of the strains was compared using Promega CytoTox 96 Non-Radioactive Cytotoxicity Assay according to manufacturer instructions (Promega, G1780). Briefly, 50 μL of supernatant was collected and combined with 50 μL substrate. Max cell lysis was measured by adding 1 mL 1.2% Triton to uninfected macrophages for 30 min and collecting 50 μL supernatant. Background absorbance was measured with 50 μL DMEM and 50 μL 1.2% Triton and these measurements were subtracted from sample absorbance values. Experiment was performed in biological triplicate and technical duplicate. Data was plotted and analyzed using GraphPad Prism 10.

Phagocytosis evasion and phagocytosed bacteria viability

Following co-culture, phagocytosis evasion of iron-limited (M9 minimal media exposure) versus iron-replete (M9 minimal media supplemented with 10 μM $Fe_2(SO_4)_3$ exposure) *K. pneumoniae* was assessed by collecting co-culture supernatant and diluting cells 10× from 10^5 – 10^9 in sterile PBS. Next, 100 μL of each dilution was plated on LB agar and incubated for 24 h at 37°C. Colony forming units (CFU) were counted to quantify viable bacteria in the culture supernatant. The viability of phagocytosed *K. pneumoniae* pre-exposed to iron-limited versus iron-replete media was assessed by lysing macrophages with 1 mL 1.2% Triton for 30 min at room temperature followed by diluting the supernatant from lysed macrophages 10× from 10^0 – 10^4 in sterile PBS and plating 100 μL of the dilutions on LB agar plates. After 24 h of static growth at 37°C, individual colonies were counted, multiplied by dilution factor and converted to CFU per milliliter. These experiments were performed in biological triplicate and technical duplicate Data was plotted and analyzed using GraphPad Prism 10.

QUANTIFICATION AND STATISTICAL ANALYSIS

For proteomics, statistical analysis included an unpaired Student's *t* test for *p*-values and multiple hypothesis testing correction by the Benjamini-Hochberg at a false discovery rate (FDR) at 5%. Quantification was performed by label-free quantification and experiments were performed in biological quadruplicate. For abundance and protein identification plots, unpaired Student's t-tests were applied with *p*-values designated as * <0.05, ** <0.01, **** <0.001. Median presented; N = number of significantly different proteins within the designated category. Precise *p*-value definitions and thresholds are reported within the main text and figure legends. For box plots, mean and standard deviation are presented.